

AD-A030 861

MASSACHUSETTS INST OF TECH LEXINGTON LINCOLN LAB

F/G 20/12

SOLID STATE RESEARCH.(U)

MAY 76 A L MCWHORTER

F19628-76-C-0002

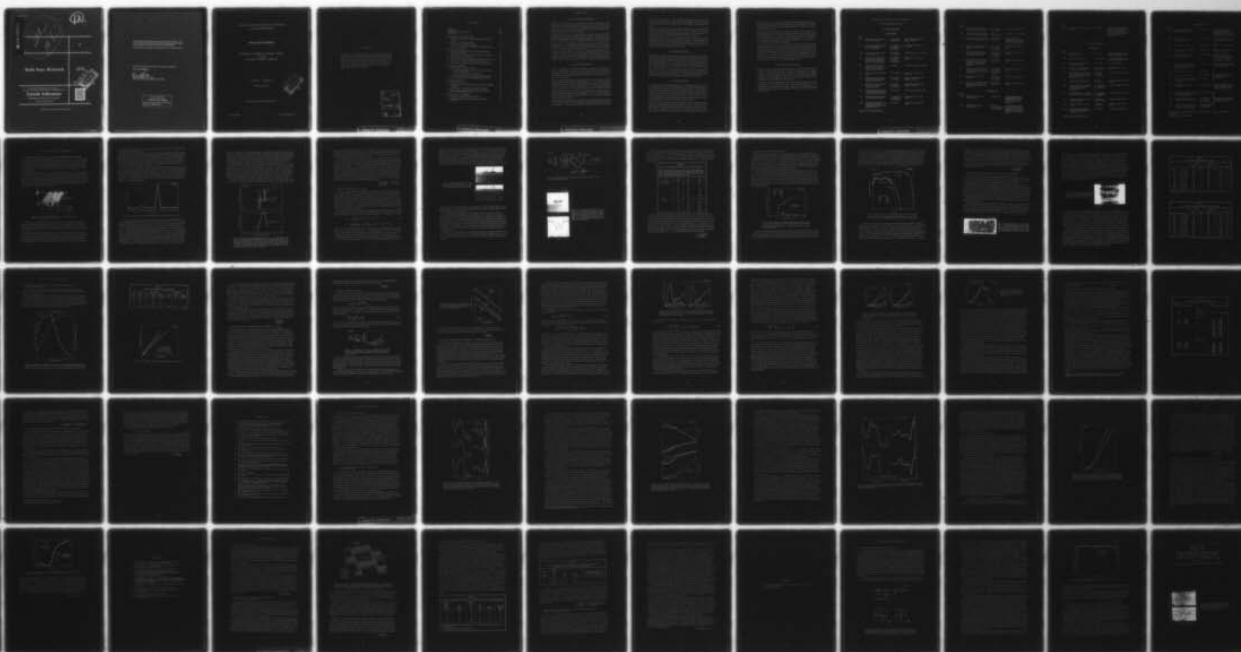
UNCLASSIFIED

TN-1975-4

ESD-TR-76-113

NL

1 OF 1
ADA030861



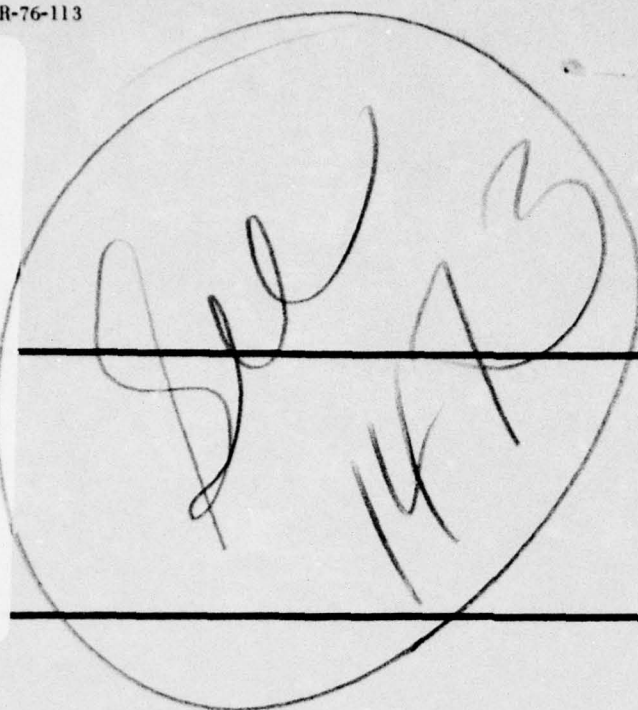
END

DATE
FILMED

11 -76

AD A030861

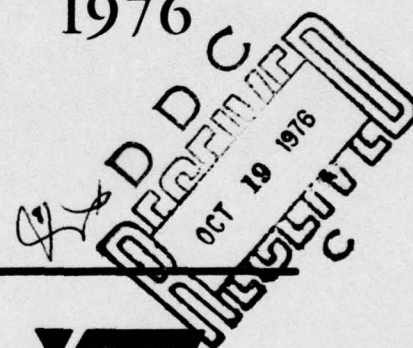
12
B.S.



2

Solid State Research

1976



Prepared for the Department of the Air Force
under Electronic Systems Division Contract F19628-76-C-0002 by

Lincoln Laboratory

MASSACHUSETTS INSTITUTE OF TECHNOLOGY

LEXINGTON, MASSACHUSETTS



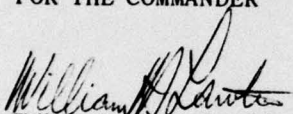
Approved for public release; distribution unlimited.

The work reported in this document was performed at Lincoln Laboratory, a center for research operated by Massachusetts Institute of Technology, with the support of the Department of the Air Force under Contract F19628-76-C-0002.

This report may be reproduced to satisfy needs of U.S. Government agencies.

This technical report has been reviewed and is approved for publication.

FOR THE COMMANDER


William H. Lawton, Lt. Col., USAF

Acting Chief, ESD Lincoln Laboratory Project Office

Non-Lincoln Recipients

PLEASE DO NOT RETURN

Permission is given to destroy this document
when it is no longer needed.

MASSACHUSETTS INSTITUTE OF TECHNOLOGY
LINCOLN LABORATORY

SOLID STATE RESEARCH

QUARTERLY TECHNICAL SUMMARY REPORT
TO THE
AIR FORCE SYSTEMS COMMAND

1 FEBRUARY - 30 APRIL 1976

ISSUED 26 JULY 1976



Approved for public release; distribution unlimited.

LEXINGTON

MASSACHUSETTS

ABSTRACT

This report covers in detail the solid state research work of the Solid State Division at Lincoln Laboratory for the period 1 February through 30 April 1976. The topics covered are Solid State Device Research, Quantum Electronics, Materials Research, Microelectronics, and Surface-Wave Technology. Funding is primarily provided by the Air Force, with additional support provided by the Army (BMDATC), ARPA (MSO, IPTO), NSF, and ERDA.

ADDITION FOR	
NTIS	Write Section <input checked="" type="checkbox"/>
D.C.	Self Section <input type="checkbox"/>
UNANNOUNCED	<input type="checkbox"/>
JUSTIFICATION	
BY	
DISTRIBUTION/AVAILABILITY CODES	
Dist.	AVAIL. NUMBER SPECIAL
A	

CONTENTS

Abstract	iii
Introduction	vii
Reports on Solid State Research	xi
Organization	xvi
 I. SOLID STATE DEVICE RESEARCH	 1
A. Distributed Feedback $\text{Pb}_{1-x}\text{Sn}_x\text{Te}$ Double-Heterostructure Lasers	1
B. GaAs $p^+n^-n^+$ Directional Couplers	4
C. Beryllium-Ion Implantation in GaAs	8
D. Improved Dicing Procedure for Pb-Salt Laser Fabrication	10
 II. QUANTUM ELECTRONICS	 15
A. Efficient High Repetition Rate Pulsed Second-Harmonic Generation in CdGeAs_2	15
B. High Peak Power Second-Harmonic Generation in CdGeAs_2	17
C. Thermal Runaway in CdGeAs_2	18
D. Infrared Third-Harmonic Generation in Phasematched CO Gas	19
E. Direct Optically Pumped Multiwavelength CO_2 Laser	25
F. Multiphoton Absorption Processes in Polyatomic Molecules	29
 III. MATERIALS RESEARCH	 33
A. Surface States on TiO_2 and SrTiO_3	33
1. Two-Dimensional Phases Associated with Defect States on the Surface of TiO_2	33
2. Electron Spectroscopy of SrTiO_3 Surfaces	39
3. Photovoltage Spectroscopy of TiO_2 and SrTiO_3 Surfaces	39
B. Selective Black Absorbers Using MgO/Au Cermet Films	41
 IV. MICROELECTRONICS	 47
A. Charge-Coupled Devices	47
B. Alignment of the 100×400 -Element Arrays for the GEODSS CCD Sensor	47
C. High-Efficiency Ion Implanted GaAs IMPATT Diodes	49
D. Double-Reticle Technique for Eliminating Photorepeated Defects in Photomasks for LSI	50
 V. SURFACE-WAVE TECHNOLOGY	 53
A. Continuously Variable-Delay-Line System	53
B. Multistrip Coupling to Surface-Acoustic-Wave (SAW) Resonators	55

INTRODUCTION

I. SOLID STATE DEVICE RESEARCH

Distributed feedback $\text{Pb}_{1-x}\text{Sn}_x\text{Te}$ stripe-geometry double-heterostructure diode lasers grown by molecular-beam epitaxy are reported with pulsed laser operation near $\lambda \approx 13.4 \mu\text{m}$. Use of the DFB laser mechanism extends the continuous tuning range of $\text{Pb}_{1-x}\text{Sn}_x\text{Te}$ for one mode from approximately 1 cm^{-1} for the Fabry-Perot mechanism, to at least 6.5 cm^{-1} for the DFB.

Stripline and channel-stop $p^+n^-n^+$ GaAs directional couplers have been fabricated and evaluated at $1.06 \mu\text{m}$ for IOC applications. Both types of couplers have exhibited 96-percent power transfer and have shown a negligible ($\sim 0.1 \text{ dB}$) insertion loss relative to a single guide having the same dimensions as one of the coupled guides.

Multiple-energy Be^+ -ion implantation techniques have been extended to higher total beryllium doses. In contrast to the results at low total beryllium doses, a significant diffusion of the implanted beryllium was observed for higher doses in GaAs.

An improved dicing or separation technique for Pb-salt laser fabrication has been investigated. The new procedure involves cutting halfway through $200\text{-}\mu\text{m}$ -thick crystals in steps of $25 \mu\text{m}$ per pass using a special high-speed saw, followed by cleaving the final $100 \mu\text{m}$. Use of this saw-cleave technique has resulted in a significant increase in the output power and device uniformity of $\text{PbS}_{1-x}\text{Se}_x$ lasers.

II. QUANTUM ELECTRONICS

In order to improve the efficiency of harmonic generation in CdGeAs_2 , the frequency-doubled output as well as direct CO_2 output were studied as a function of Q-switching frequency. With the use of a new chopper wheel and improved laser mode quality, average and peak doubling efficiencies of 20.5 and 30.4 percent, respectively, were obtained.

In a study aimed at obtaining high single-pulse energy, 0.2 J of doubled CO_2 TEA laser output has been obtained from an uncoated $8 \times 12 \times 11\text{-mm}^2$ crystal of CdGeAs_2 . Antireflection-coated crystals have given 27-percent external energy conversion efficiency in a 12-mm length, with a 70-nsec TEM_{00} laser pulse. Coated crystals show a 10- to 20-percent decrease in surface damage threshold.

Calculations have been made of the critical average power level for thermal runaway in CdGeAs_2 as a function of bath temperature. The critical power is typically of the order of a few watts at room temperature, and is two orders of magnitude higher at nitrogen temperature.

Phasematched third-harmonic generation of CO_2 laser radiation has been carried out in CO and NO using a small concentration of SF_6 to provide compensatory positive dispersion. In the present experiments, conversion efficiencies as high as

2×10^{-8} have been observed. Based upon these results and theoretical calculations, a conversion efficiency of 10 percent should be possible for a 24-m cell and a 1-nsec laser pulse having an energy below the gas breakdown and window damage limits.

An HF laser was used to directly pump various isotopes of CO_2 . Intense lasing was observed on numerous lines in the 4.3-, 10.6-, and 17- μm regions. All observed 4.3- and 17- μm CO_2 laser emission lines were assigned. Pressure dependence of lasing spectra and laser pulse temporal features were also examined.

Spectrophone measurements have been made of absorption in SF_6 near 10 μm with a step-tunable CO_2 . As the laser intensity is increased, the absorption spectrum broadens toward lower frequencies, and subsidiary maxima occur. The results are consistent with a multiphoton absorption model where vibrational anharmonicity is partially compensated by rotational energy changes.

III. MATERIALS RESEARCH

Surface states on TiO_2 and SrTiO_3 play a key role in the photoelectrolysis of water in cells with anodes made from these semiconductors. The origin and behavior of these states are being investigated by the complementary techniques of electron and photovoltage spectroscopy. From the electron spectra of TiO_2 surfaces that have been bombarded with Ar ions, one can infer the existence of three different surface defect phases, depending on the concentration of defects produced by bombardment.

Selective black absorbers with solar absorptivities of over 90 percent and infrared emissivities of less than 10 percent have been prepared by depositing sputtered MgO/Au cermet films on metal substrates. For films deposited on stainless steel coated with molybdenum, the optical properties remain stable up to 400°C.

IV. MICROELECTRONICS

To evaluate the benefit of phosphorous gettering in lowering the dark current in the CCD imaging arrays for the GEODSS (Ground Electro-Optical Deep Space Surveillance) Program, the actual dark current for gettered devices was measured and correlated with dark currents determined from measurements on a gated diode included on each chip. On the two devices tested, dark currents of 27 and 36 nA/cm^2 were measured on the CCD as compared to values of 18 and 35 nA/cm^2 , respectively, determined from gated-diode measurements, giving confidence to gated-diode measurements as indicators of average CCD dark current.

The sensor being developed for use at the prime focus of the GEODSS Program telescope is a hybrid integrated circuit containing 16 CCD 100- \times 400-element imaging arrays. The alignment requirements for this sensor are such that a vertical row of sensing elements on any one chip must align within 0.0004 inch with the same column on all devices above and below it, and the element arrays must be

parallel to within 0.03° . A measuring coordinator has been modified so that its inherent accuracy can be utilized in chip placement, and 16 mechanical devices have been placed down using this coordinator within the required 0.0004-inch tolerance in both the x and y axes.

A DC-to-RF conversion efficiency of 37 percent combined with an output power of 3.4 W has been obtained at 3.3 GHz from a Schottky-barrier GaAs IMPATT diode having an implanted lo-hi-lo profile. The donor spike was produced by implanting silicon into an epitaxial layer with an n-type concentration of $1.65 \times 10^{15} \text{ cm}^{-3}$. This implantation technique has resulted in a very high yield of lo-hi-lo profile devices with efficiencies greater than 30 percent.

In order to minimize the effect of defects on the 10X reticle used for generating LSI masks and to reduce the amount of reticle inspection and cleaning required, we have devised a technique of re-exposing the clear areas of the mask using a second reticle with slightly larger geometries. The second exposure removes the images caused by dirt or gel slugs on the first reticle, except immediately adjacent to the patterns. This technique has been used for the fabrication of masks for the Lincoln ECL Gate Array. Reticles with heretofore unusable defect densities were used to generate usable masks with two or less photorepeated defects.

V. SURFACE-WAVE TECHNOLOGY

Surface-acoustic-wave (SAW) dispersive delay lines in the RAC (reflective-array-compressor) configuration have been developed and incorporated in a voltage-controlled continuously variable delay-line system. This system will be evaluated for potential use in a multipath canceller in the LES-10 satellite communications program. The variable delay-line system provides a differential delay of 30 μsec and has a bandwidth of 10 MHz centered at 70 MHz.

The behavior of a SAW multistrip coupler in a standing-wave environment has been investigated with the use of a SAW resonator. The measured response is in excellent agreement with a model of the combined coupler and resonator response. An understanding of this behavior is important to the design of multistrip coupled-resonator filters.

REPORTS ON SOLID STATE RESEARCH

15 February through 15 May 1976

PUBLISHED REPORTS

Journal Articles

JA No.

- | | | | |
|------|--|---|---|
| 4461 | External Cavity CO ₂ -Pumped InSb Spin-Flip Laser | S. R. J. Brueck
A. Mooradian | IEEE J. Quantum Electron. <u>QE-12</u> , 201 (1976) |
| 4465 | Molecular Absorption of Infra-red Laser Radiation in the Natural Atmosphere | P. L. Kelley
R. A. McClatchey*
R. K. Long*
A. Snelson* | Opt. Quantum Electron. <u>8</u> , 117 (1976) |
| 4508 | Electrical Characterization of Epitaxial Layers | G. E. Stillman
C. M. Wolfe | Thin Solid Films <u>31</u> , 69 (1976) |
| 4512 | Low-Loss High-Purity GaAs Waveguides for Monolithic Integrated Optical Circuits at GaAs Laser Wavelengths | G. E. Stillman
C. M. Wolfe
J. A. Rossi
H. Heckscher | Appl. Phys. Lett. <u>28</u> , 197 (1976) |
| 4519 | High-Resolution Methane ν_3 -Band Spectra Using a Stabilized Tunable Difference-Frequency Laser System | A. S. Pine | J. Opt. Soc. Am. <u>66</u> , 97 (1976) |
| 4521 | Optically Pumped 16- μ m CO ₂ Laser | R. M. Osgood, Jr. | Appl. Phys. Lett. <u>28</u> , 342 (1976) |
| 4540 | Output Coupling for Closely Confined Pb _{1-x} Sn _x Te Double-Heterostructure Lasers | R. W. Davies
J. N. Walpole | IEEE J. Quantum Electron. <u>QE-12</u> , 291 (1976) |
| 4545 | Spiking Oscillations in Diode-Pumped NdP ₅ O ₁₄ and NdAl ₃ (BO ₃) ₄ Lasers | S. R. Chinn
H. Y-P. Hong
J. W. Pierce | IEEE J. Quantum Electron. <u>QE-12</u> , 189 (1976) |
| 4552 | Inhomogeneous Broadening of the Lyman-Series Absorption of Simple Hydrogenic Donors | D. M. Larsen | Phys. Rev. B <u>13</u> , 1681 (1976) |
| 4553 | Photoelectrolysis of Water in Cells with SrTiO ₃ Anodes | J. G. Mavroides
J. A. Kafalas
D. F. Kolesar | Appl. Phys. Lett. <u>28</u> , 241 (1976) |
| 4554 | Room-Temperature Operation of GaInAsP/InP Double-Heterostructure Diode Lasers Emitting at 1.1 μ m | J. J. Hsieh | Appl. Phys. Lett. <u>28</u> , 283 (1976) |

* Author not at Lincoln Laboratory.

JA No.

- | | | | |
|-------|---|---|--|
| 4555A | Transparent Heat Mirrors
for Solar-Energy Applications | J. C. C. Fan
F. J. Bachner | Appl. Opt. <u>15</u> , 1012 (1976) |
| 4557 | Lattice Dynamics of Transition
Metals in the Resonance Model | B. A. Oli
A. O. E. Animalu | Phys. Rev. B <u>13</u> , 2398 (1976) |
| 4561 | Fabrication of Silicon MOS De-
vices Using X-Ray Lithography | S. E. Bernacki
H. I. Smith | NIKKEI Electronics
(Erekutoronikusu), Japan.
No. 125, 139-157 (12 Janu-
ary 1976) (in Japanese) |
| 4567 | Thin-Film Conducting Micro-
grids as Transparent Heat
Mirrors | J. C. C. Fan
F. J. Bachner
R. A. Murphy | Appl. Phys. Lett. <u>28</u> , 440
(1976) |
| 4571 | Electroabsorption in GaAs and
Its Application to Waveguide
Detectors and Modulators | G. E. Stillman
C. M. Wolfe
C. O. Bozler
J. A. Rossi | Appl. Phys. Lett. <u>28</u> , 544
(1976) |
| 4572 | Crystal Structure and Fluores-
cence Lifetime of Potassium
Neodymium Orthophosphate,
$K_3Nd(PO_4)_2$, a New Laser
Material | H. Y-P. Hong
S. R. Chinn | Mater. Res. Bull. <u>11</u> , 421
(1976) |
| 4592 | Double-Heterostructure PbSnTe
Lasers Grown by Molecular-
Beam Epitaxy with cw Operation
Up to 114 K | J. N. Walpole
A. R. Calawa
T. C. Harman
S. H. Groves | Appl. Phys. Lett. <u>28</u> , 552
(1976) |
| 4593 | Minilasers of Neodymium
Compounds | S. R. Chinn
H. Y-P. Hong
J. W. Pierce | Laser Focus <u>12</u> , 64 (1976) |
| 4614 | Influence of Local-Site Symmetry
on Fluorescence Lifetime in
High-Nd-Concentration Laser
Materials | H. Y-P. Hong
S. R. Chinn | Mater. Res. Bull. <u>11</u> , 461
(1976) |

Meeting SpeechesMS No.

- | | | | |
|-------|--|--|--|
| 3337O | High Resolution Tunable
Infrared Lasers | A. Mooradian | In <u>Very High Resolution
Spectroscopy</u> , edited by
R. A. Smith (Academic
Press, London, 1976),
pp. 75-89 |
| 3983 | High-Efficiency Electro-
chemical Plant | M. S. Hsu
W. E. Morrow, Jr.
J. B. Goodenough | Tenth Intersociety Energy
Conversion Engineering
Conference, University of
Delaware, 17-22 August
1975 (IECEC '75 Record),
p. 555 |

MS No.

4094	GaAs-Based Integrated Optical Circuits	I. Melngailis	Proceedings of the Technical Program, Electro-optical Systems Design Conference - 1975, International Laser Exposition, Anaheim, California, 11-19 November 1975, pp. 453-459
------	--	---------------	---

* * * * *

UNPUBLISHED REPORTS

Journal Articles

JA No.

4486	Surface Wave Device Fabrication	H. I. Smith	Accepted as Chapter 4 in <u>Surface Wave Devices</u> (Wiley)
4505	Reflection-Grating Devices	R. C. Williamson	Accepted as Chapter 9 in <u>Surface Wave Devices</u> (Wiley)
4570	Thermal Faceting of (110) and (111) Surfaces of MgO	V. E. Henrich	Accepted by Surf. Sci.
4576	Vibrational Energy Relaxation in Liquid N ₂ -CO Mixtures	S. R. J. Brueck R. M. Osgood, Jr.	Accepted by Chem. Phys. Lett.
4584	Room-Temperature, cw Operation of GaInAsP/InP Double-Heterostructure Diode Lasers Emitting at 1.1 μ m	J. J. Hsieh J. A. Rossi J. P. Donnelly	Accepted by Appl. Phys. Lett.
4585	Infrared Third Harmonic Generation in Molecular Gases	H. Kildal T. F. Deutsch	Accepted by IEEE J. Quantum Electron.
4601	Uniform-Carrier-Concentration p-Type Layers in GaAs Produced by Beryllium Ion Implantation	J. P. Donnelly F. J. Leonberger C. O. Bozler	Accepted by Appl. Phys. Lett.
4604	Low-Loss GaAs p ⁺ n ⁻ n ⁺ Three-Dimensional Optical Waveguides	F. J. Leonberger J. P. Donnelly C. O. Bozler	Accepted by Appl. Phys. Lett.
4616	Excitation of Polyatomic Molecules by Radiation	D. M. Larsen N. Bloembergen*	Accepted by Opt. Commun.
4617	A Reexamination of the CS ₂ Laser	T. F. Deutsch H. Kildal	Accepted by Chem. Phys. Lett.
MS-3986	Planar HgCdTe Quadrantal Heterodyne Arrays with GHz Response at 10.6 μ m	D. L. Spears	Accepted by Infrared Phys.

* Author not at Lincoln Laboratory.

Meeting Speeches*

MS No.

4059B, C	Photoelectrolysis of Water on Semiconducting Surfaces	D. I. Tchernev	Thirteenth Space Congress, Cocoa Beach, Florida, 7-9 April 1976; Seminar, Raytheon Company, Waltham, Massachusetts, 10 March 1976
4060A	Photoelectrolysis of Water by Solar Energy	D. I. Tchernev	Chemistry Seminar, University of Pittsburgh, 25 March 1976
4067E	Applications of Tunable Laser	A. Mooradian	Seminar, M.I.T., 4 March 1976
4067F	Recent Advances in Tunable Infrared Lasers	A. Mooradian	Seminar, Kodak, Rochester, New York, 6 May 1976
4136C	Ceramics for Energy Conservation and Storage	J. B. Goodenough	Electrochemical Society Meeting, Ledgemont Laboratory, Kennecott Copper Corporation, Lexington, Massachusetts, 13 April 1976
4139	Room-Temperature Operation of GaInAsP/InP Double-Heterostructure Diode Lasers Emitting at 1.1 μm	J. J. Hsieh	Topical Meeting on Integrated Optics, Salt Lake City, Utah, 12-14 January 1976
4177	Wavelength-Selective Surfaces	J. C. C. Fan	} American Chemical Society Meeting, New York, 4-9 April 1976
4178	New Solid Electrolytes	H. Y-P. Hong	
4179	Efficiencies of Methanol Manufacture from Gas, Coal, Waste and Wood	T. B. Reed	
4195	Ion Implantation in Semiconductors	J. P. Donnelly	Meeting of Electron Device Group of Boston Section of IEEE, Burlington, Massachusetts, 17 March 1976
4197	Surface Loss-Functions and Electronic Structure of Titanium and Vanadium Oxides	A. O. E. Animalu	} American Physical Society Meeting, Atlanta, Georgia, 29 March - 1 April 1976
4198	Relative Stability of O^{2-} and O^- Ions on Crystal Surfaces	G. Dresselhaus H. J. Zeiger V. E. Henrich	
4199	Graphite Intercalation Compounds IV. Density of States Model for Dilute Compounds	M. S. Dresselhaus [†] G. Dresselhaus J. E. Fischer [†]	

*Titles of Meeting Speeches are listed for information only. No copies are available for distribution.

[†] Author not at Lincoln Laboratory.

MS No.			
4200	Soft Phonon Modes and d-band Resonance in Vanadium	B. A. Oli A. O. E. Animalu	American Physical Society Meeting, Atlanta, Georgia, 29 March - 1 April 1976
4201	Raman Scattering Tensors in Cubic Magnetic Semiconductors	S. A. Safran* G. Dresselhaus M. S. Dresselhaus* B. Lax*	
4205	Design of Reflective-Array Surface Wave Devices	J. Melngailis R. C. Williamson J. Holtham R. C. M. Li	Accepted by Special Issue of Wave Electronics, Bologna, Italy
4232	Transparent Heat Mirrors for Solar-Energy Applications	J. C. C. Fan	World Fair for Technology Exchange, Chicago, 4 February 1976
4233	Ion Implanted Lo-Hi-Lo Profile IMPATT Diodes	C. O. Bozler J. P. Donnelly R. A. Murphy R. W. Laton R. W. Sudbury W. T. Lindley	WOCSEMMAD '76, San Diego, 11-12 March 1976
4238A	Preparation of Polycrystalline Si Thin Films by Laser Crystallization	J. C. C. Fan	American Vacuum Society Symposium, Yorktown Heights, New York, 6 April 1976
4251	Far Infrared Emission by Optical Pumping of Molecules	H. R. Fetterman	Seminar, M.I.T., 18 March 1976
4264	Lasers for Isotope Separation	A. Mooradian T. F. Deutsch H. R. Fetterman C. Freed G. Iseler H. Kildal N. Menyuk R. M. Osgood, Jr.	Conference on Lasers for Isotope Separation, Albuquerque, 13-14 April 1976
4265	Lasing and Fluorescence in High-Nd-Concentration Materials	S. R. Chinn	Seminar, IBM Watson Research Center, Yorktown Heights, New York, 12 April 1976
4278	Energy Research at M.I.T. Lincoln Laboratory	A. O. E. Animalu	Seminar, Howard University, Washington, D.C., 21 April 1976

* Author not at Lincoln Laboratory.

ORGANIZATION

SOLID STATE DIVISION

A. L. McWhorter, *Head*
I. Melngailis, *Associate Head*
C. R. Grant, *Assistant*
P. E. Tannenwald

QUANTUM ELECTRONICS

A. Mooradian, *Leader*
P. L. Kelley, *Associate Leader*

Barch, W. E.	Heckscher, H.
Brueck, S. R. J.	Kildal, H.
Burke, J. W.	Larsen, D. M.
Chinn, S. R.	Menyuk, N.
DeFeo, W. E.	Moulton, P. F.
Deutsch, T. F.	Osgood, R. M.
Fetterman, H. R.	Parker, C. D.
Hancock, R. C.	Pine, A. S.

ELECTRONIC MATERIALS

J. B. Goodenough, *Leader*
A. J. Strauss, *Associate Leader*

Anderson, C. H., Jr.	LaFleur, W. J.
Animalu, A. O. E.	Mastromattei, E. L.
Button, M. J.	Mavroides, J. G.
Delaney, E. J.	Mroczkowski, I. H.
Dresselhaus, G.	Oli, B. A.*
Dwight, K., Jr.	Owens, E. B.
Fahey, R. E.	Palm, B. J.
Fan, J. C. C.	Pantano, J. V.
Feldman, B.	Pierce, J. W.
Finn, M. C.	Plonko, M. C.
Henrich, V. E.	Reed, T. B.
Hong, H. Y-P.	Tchernev, D. I.
Hsieh, J. J.	Tracy, D. M.
Iseler, G. W.	Vohl, P.
Kafalas, J. A.	Zavracky, P. M.
Kolesar, D. F.	Zeiger, H. J.
Krohn, L., Jr.	

APPLIED PHYSICS

A. G. Foyt, *Leader*
T. C. Harman, *Assistant Leader*
C. E. Hurwitz, *Assistant Leader*

Belanger, L. J.	Lind, T. A.
Calawa, A. R.	McBride, W. F.
Carter, F. B.	Orphanos, W. G.
DeMeo, N. L., Jr.	Paladino, A. E.
Donnelly, J. P.	Rossi, J. A.
Ferrante, G. A.	Spears, D. L.
Groves, S. H.	Tsang, D. Z.*
Leonberger, F. J.	Walpole, J. N.

SURFACE WAVE TECHNOLOGY

E. Stern, *Leader*
R. C. Williamson, *Assistant Leader*

Alusow, J. A.	Kernan, W. C.
Brogan, W. T.	Li, R. C. M.
Cafarella, J. H.	Melngailis, J.
DeGraff, P. D.	Ralston, R. W.
Dolat, V. S.	Reible, S. A.
Efremow, N., Jr.	Smith, H. I.
Flanders, D. C.*	Vlannes, N.*

MICROELECTRONICS

W. T. Lindley, *Leader*
F. J. Bachner, *Assistant Leader*

Beatrice, P. A.	Gray, R. V.
Bozler, C. O.	Lincoln, G. A., Jr.
Burke, B. E.	McGonagle, W. H.
Clifton, B. J.	Mountain, R. W.
Clough, T. F.	Murphy, R. A.
Cohen, R. A.	Pichler, H. H.
Durant, G. L.	Smythe, D. L., Jr.
Foley, G. H.	Wilde, R. E.
Grant, L. L.	

* Research assistant

I. SOLID STATE DEVICE RESEARCH

A. DISTRIBUTED FEEDBACK $\text{Pb}_{1-x}\text{Sn}_x\text{Te}$ DOUBLE-HETEROSTRUCTURE LASERS

We report distributed feedback¹ (DFB) pulsed laser operation near $\lambda \approx 13.4\text{-}\mu\text{m}$ wavelength in stripe-geometry $\text{Pb}_{1-x}\text{Sn}_x\text{Te}$ double heterostructures (DH) grown by molecular-beam epitaxy. Since the DFB mechanism yields highly frequency-selective devices in which the total output power may be in one or two modes, DFB operation in this alloy system is particularly significant for tunable local oscillator applications in optical systems operating in the 8- to 12- μm atmospheric window.

Previous DFB injection lasers have been operated exclusively near 0.9 μm in the $\text{Al}_x\text{Ga}_{1-x}\text{As}$ alloy system.² Because of the longer wavelength of emission in $\text{Pb}_{1-x}\text{Sn}_x\text{Te}$, the DFB grating of the devices discussed here (1.1- μm periodicity) can easily be made to operate in the first Bragg order rather than in the higher orders frequently used in $\text{Al}_x\text{Ga}_{1-x}\text{As}$. Also, as discussed below, a relatively simple DH structure can be used in $\text{Pb}_{1-x}\text{Sn}_x\text{Te}$ to achieve a large coupling coefficient κ (Ref. 1) for Bragg reflection without locating the grating at a hetero-interface or using multilayered, separate confinement structures.

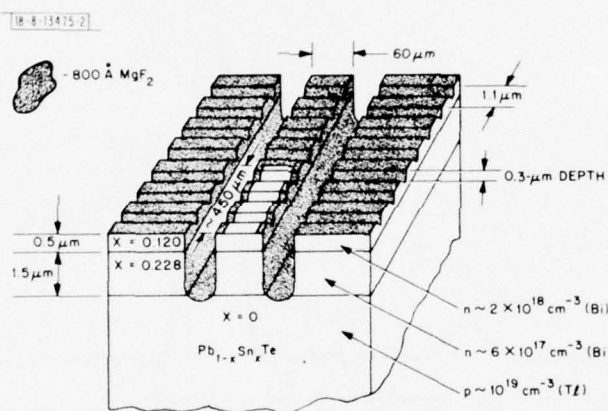


Fig. I-1. Schematic of DFB double-heterostructure $\text{Pb}_{1-x}\text{Sn}_x\text{Te}$ laser without metallization. See text.

The structure used is shown schematically in Fig. I-1. The present devices differ very little in their structure (except for the grating) from the DH $\text{Pb}_{1-x}\text{Sn}_x\text{Te}$ lasers reported recently³ having conventional Fabry-Perot cavities. The type of substrates used, the epitaxial growth parameters, the dopants and their concentrations are all identical to the previous Fabry-Perot lasers.

The grating was fabricated over the entire surface of the top layer after all epitaxy was completed. This was accomplished by exposing a 1000- \AA layer of Shipley AZ 1350J photoresist to interference fringes formed by splitting a 0.4579- μm argon laser beam into two equally intense beams which were recombined on the surface of the photoresist at the desired angle.⁴ After developing the resist, the sample was RF sputter-etched with argon ions. The etch rate

for the PbTe was $250 \text{ \AA}/\text{min.}$, compared with $30 \text{ \AA}/\text{min.}$ for the resist. The remaining resist was removed by plasma oxidation.

Because the last epitaxial layer can be made very thin without introducing significant optical loss for TE modes, as has been shown previously,⁵ and because the sputtering parameters and grating spacing allow etching to almost any desired depth in this layer, very large coupling can be achieved. In cross section, the grating etched here is $0.3 \text{ }\mu\text{m}$ deep and has a trapezoidal shape with roughly equal peak and valley widths. For this grating on the structure in Fig. I-1 we calculate the fundamental Fourier component of the variation in guide index to be $n_1 \approx 0.08$, which leads to an estimated coupling coefficient¹ $\kappa \approx 190 \text{ cm}^{-1}$.

A stripe geometry was obtained by sputter-etching striped channels through the active layer which isolated $60\text{-}\mu\text{m}$ -wide striped mesas. An $800\text{-}\text{\AA}$ layer of MgF_2 was deposited and patterned so that rectangular openings in the insulator with dimensions of $50 \times 500 \text{ }\mu\text{m}^2$ were obtained on top of the striped mesas. After metallization, devices were cut with a high-speed diamond saw to lengths of $900 \text{ }\mu\text{m}$ along the stripe. The uninsulated length (region of electrical injection, and hence gain) after cutting was at one end of the mesa, leaving a nearly equal, electrically insulated (passive) length at the other end.

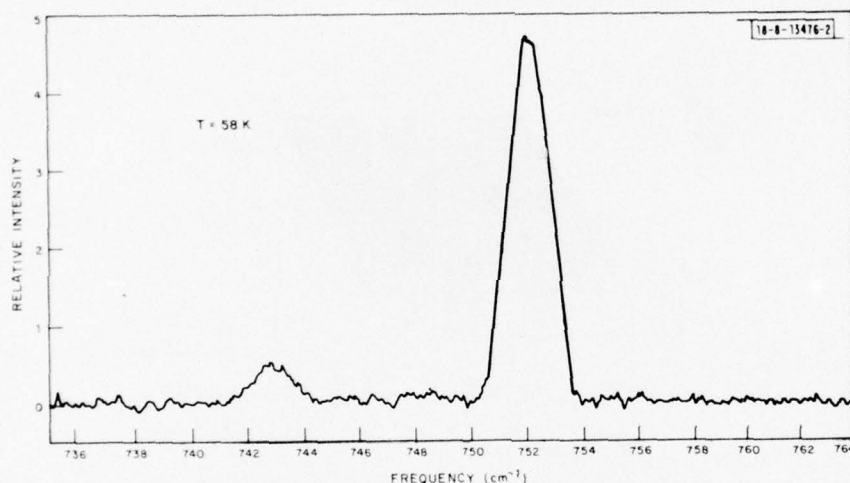


Fig. I-2. Pulsed emission spectrum of DFB laser at 58-K heat-sink temperature.

The devices were tested for laser emission in a closed-cycle cryogenic refrigerator with heat-sink temperatures between 12 and 80 K. Current pulses of 8 A ($\sim 25 \text{ kA}/\text{cm}^2$), of $0.5\text{-}\mu\text{sec}$ duration, and of 6 kHz repetition rate were applied. A spectrum of the emission observed at 58-K heat-sink temperature is shown in Fig. I-2. Only two modes were seen separated by $\sim 9 \text{ cm}^{-1}$, with the amplitude of the higher frequency mode a factor of 9 times larger than the other. As the heat-sink temperature was varied from 38 to 62.5 K, these two modes tuned continuously and maintained their spacing and amplitude relative to each other. The mode frequencies vs heat-sink temperature for a DFB laser are compared in Fig. I-3(a) with data for one of the Fabry-Perot cavity (FP) lasers of similar structure and dimensions, and under similar pulsed conditions. Estimates of the thermal characteristics of the devices indicate that the temperature of the active region of the structure rises 25 to 50 K above the heat-sink temperature during the pulse, so that the spontaneous line tunes (or "chirps") by 100 to 200 cm^{-1} .

Because of the large, time-dependent difference in temperature between the active layer and the heat sink, it is difficult to interpret the tuning rate of the DFB modes with respect to heat-sink temperature. The observed rate of $\sim 0.25 \text{ cm}^{-1}/\text{K}$, however, is comparable to or smaller than the index tuning of FP modes with heat-sink temperature under constant DC excitation, and is much smaller than the spontaneous-line tuning rate, $\sim 3.2 \text{ cm}^{-1}/\text{K}$, indicated in Fig. I-3(a) by the line labeled slope = dE_g/dT . The tuning range of the strong mode is $\sim 6.5 \text{ cm}^{-1}$.

The pulsed FP laser emission modes at heat-sink temperatures of 45 and 58 K are shown for comparison. There are numerous modes spread over $\sim 60 \text{ cm}^{-1}$. One mode at 45 K and two nearly-equal modes at 58 K are much stronger than the remainder. These are marked by asterisks in Fig. I-3(a) and correspond roughly to the maximum of the time-averaged spontaneous lineshape (or gain) vs frequency, as can be seen by comparison with the line of slope dE_g/dT . Only data at two temperatures are shown for clarity. However, similar multimode output of nearly constant total intensity was observed throughout the heat-sink-temperature range.

In contrast, the DFB laser showed emission only over a limited temperature range, as indicated in Fig. I-3(b) where the relative amplitude of the strong DFB mode (essentially the total

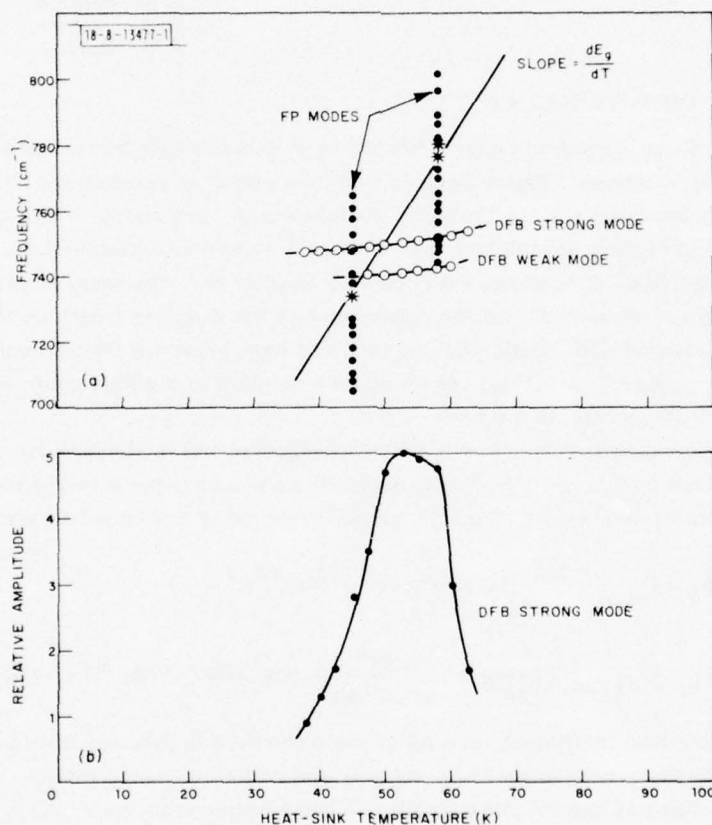


Fig. I-3. (a) Frequency of pulsed DFB laser modes vs heat-sink temperature (open circles) compared with pulsed laser modes from similar FP device at 45 and 58 K (solid circles). Asterisks indicate strongest FP emission, and show approximate tuning rate of spontaneous emission given by dE_g/dT . (b) Relative amplitude of strong DFB mode vs heat-sink temperature. No emission is observed below 20 K for DFB laser, as opposed to FP laser which has nearly constant emission intensity.

output) is shown vs heat-sink temperature. No emission at all was observed for $T \lesssim 20$ K, and the emission was sufficiently strong to easily measure the spectra only between 38 and 62.5 K. Only in this range can the Bragg condition be met for any significant time during the pulse as the index and spontaneous line are temperature-tuned.

If we assume that the Bragg frequency is $\nu_0 \approx 745 \text{ cm}^{-1}$, near the center of the two modes seen, we obtain a guide index $n_g \approx 6.1$, in good agreement with theoretical calculations for this structure. The presence of two lowest-order modes is predicted theoretically¹ for index modulation; in the overcoupled (or low-gain) approximation (and neglecting dispersion), they would be located at frequencies $\nu \approx \nu_0 \pm \kappa c / 2\pi n_g$, having a separation (using our estimates for the coupling parameter and guide index) consistent with the 9-cm^{-1} separation observed. The difference in intensities might arise from mode competition and saturation effects in the lasing regime. Another possible origin of the second mode might be from the effect of the passive grating region, which could have appreciable reflectivity at a different frequency since its effective index and, hence, Bragg frequency probably differ significantly from the active-region index and center frequency due to the difference in temperatures.

J. N. Walpole S. H. Groves
A. R. Calawa T. C. Harman
S. R. Chinn

B. GaAs $p^+n^-n^+$ DIRECTIONAL COUPLERS

Two types of GaAs directional couplers have been successfully fabricated and evaluated at $1.06 \mu\text{m}$ for IOC applications. These devices would be useful as passive power dividers, and also as potential structures for electro-optic switches (e.g., see Ref. 6). The couplers were made from a pair of closely spaced low-loss ($\sim 1 \text{ cm}^{-1}$ at $1.06 \mu\text{m}$) single-mode $p^+n^-n^+$ three-dimensional waveguides.⁷ Structures with coupling lengths (for maximum power transfer) from 4 to 24 mm have been evaluated, and the dependence of the coupling length on the device dimensions has been characterized. Both types of couplers have exhibited 96-percent power coupling, and have shown a negligible (~ 0.1 dB) insertion loss relative to a single guide having the same dimensions as one of the coupled guides.

A directional coupler is formed by parallel waveguides and is characterized by the exchange of power between the guided modes. From coupled-mode theory for a two-guide coupler, the interguide distribution of power P_0 initially coupled into guide b at $z = 0$ is given for $z > 0$ by⁶

$$P_a = P_0 \frac{4K^2}{4K^2 + (\Delta\beta)^2} \sin^2 \{ [4K^2 + (\Delta\beta)^2]^{1/2} z/2 \} \quad (\text{I-1})$$

$$P_b = P_0 \left(\frac{(\Delta\beta)^2}{4K^2 + (\Delta\beta)^2} + \frac{4K^2}{4K^2 + (\Delta\beta)^2} \cos^2 \{ [4K^2 + (\Delta\beta)^2]^{1/2} z/2 \} \right) \quad (\text{I-2})$$

where K is the coupling coefficient, and $\Delta\beta$ is the difference in propagation constants between the two guides. In the synchronous case, $\Delta\beta = 0$, and complete power transfer occurs in a distance $L = \pi/2K$ defined as the coupling length. In the asynchronous case, $\Delta\beta \neq 0$, and both the coupling length and the maximum power transfer are less than for the synchronous case.

We have fabricated $p^+n^-n^+$ directional couplers formed by a pair of identical optical strip-lines^{7,8} or channel-stop strip guides.^{7,9} In both cases, the guide spacing was about $3 \mu\text{m}$. The

structures consist of an $n^+(10^{18} \text{ cm}^{-3})$ substrate, an $n^-(\sim 10^{14} \text{ cm}^{-3})$ epitaxial layer with initial thickness in the 5- to 8- μm range, and ion-implanted $p^+(3 \times 10^{18} \text{ cm}^{-3})$ regions to laterally confine the light. The fabrication techniques for the couplers are similar to those for the single guides described previously.⁷⁻⁹ It is worth noting that multiple-energy Be^+ implantations (see Ref. 10, and p. 8 in Ref. 9) were used to form p^+ regions of uniform concentration (and thus of uniform refractive index) to a depth of about 1.5 μm , with a junction 2 μm from the surface. Figure I-4(a-b) shows photomicrographs of cleaved cross sections of the stripline and the channel-stop couplers. The cleaved faces have been treated with a stain/etchant¹¹ to reveal the

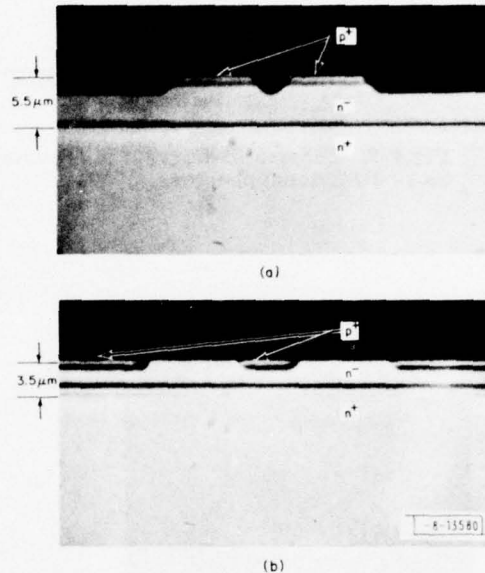


Fig. I-4. Photomicrographs of cleaved and stained cross sections of GaAs $p^+n^-n^+$ (a) stripline directional coupler and (b) channel-stop directional coupler.

high-concentration p^+ regions and the n^-n^+ growth interface. In the stripline coupler, light is guided beneath the p^+ ribs, while in the planar channel-stop coupler, light is guided in the two channels between the three p^+ regions.

The experimental arrangement for evaluating the couplers is shown schematically in Fig. I-5. The TE-polarized radiation from a Nd:YAG laser was focused on one guide at the cleaved input face of the coupler. For qualitative evaluation, a magnified image formed on an infrared vidicon of the near-field intensity pattern at the coupler output face was displayed on a television monitor. The relative power in each channel was usually determined by scanning the output-face image across a slit opening in front of a detector, and displaying the resulting photosignal on an oscilloscope. For cases in which the majority of the light emerged from a single guide, a phase-sensitive detection method was used to measure the power division between the channels.

Figure I-6(a-b) shows the typical output intensity pattern from a channel-stop coupler, and the corresponding oscilloscope trace. The guides are 15 μm wide, and the sample is 7.8 mm long. The input laser radiation is focused on the guide to the left, and about 3-dB coupling is observed.

18-8-13555-1

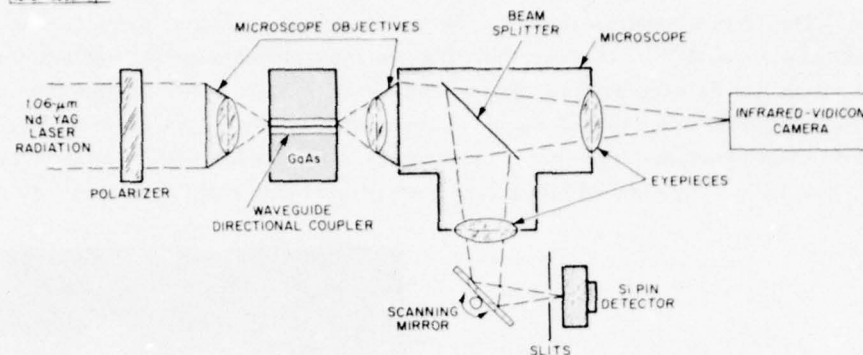
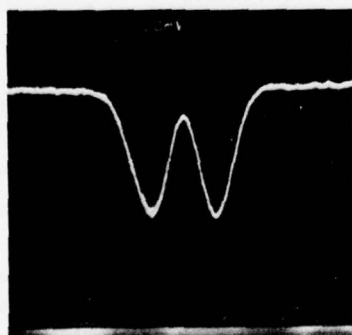


Fig.1-5. Schematic diagram of experimental arrangement used to evaluate GaAs directional couplers.

-8-13581



(a)



(b)

Fig.1-6. (a) Near-field intensity pattern at output face of channel-stop coupler. Entire output face has been illuminated for clarity. Input laser radiation is focused on left guide; guides are 15 μm wide, and sample is 7.8 mm long. (b) Corresponding oscilloscope trace obtained by scanning near-field image across slits in front of detector.

As high as 96-percent power coupling has been measured in samples 8 to 10 mm long for both stripline and channel-stop couplers having 10- μ m-wide guides. From Eq. (I-2), this implies a value for $\Delta\beta/\beta \approx 4 \times 10^{-6}$, indicating that these couplers are highly synchronous. This result shows that it is reasonable to set $\Delta\beta = 0$ in Eqs. (I-1) and (I-2), and to uniquely determine the coupling length from the simplified equations using coupling data for several lengths of the same sample.

TABLE I-1 GaAs p ⁺ n ⁻ n ⁺ DIRECTIONAL-COUPLER OPTICAL CHARACTERISTICS			
Here w is the width of one guide, t is the initial and final epitaxial layer thickness for the channel-stop and stripline couplers, respectively, and L is the coupling length. The uncertainty in L is ≤ 5 percent unless otherwise noted. The guide spacing is about 3 μ m in all cases.			
Type	w (μ m)	t (μ m)	L (mm)
Channel-stop	5	4.2	4.2
	5	5.2	4.1
	10	4.2	7.8
	10	5.2	7.9
	15	4.2	15.0
	15	5.2	14.2
Stripline	10	3.4	11.5
	10	5.0	9.9 \pm 0.8
	15	3.4	24.2
	15	5.0	22.3
	15	5.9	20.5

The measured coupling lengths are summarized in Table I-1. It is evident that for the wider guides the coupling lengths are longer; this is because the mode is better confined, and there is less evanescent-tail penetration to the adjacent guide. For the stripline couplers, the coupling length increases about 20 percent as the epitaxial layer thickness decreases from 5.9 to 3.4 μ m; this also is attributable to improved mode confinement. The measurement uncertainty in these L values is about 5 percent; it should be noted that including the $\Delta\beta$ terms introduces only a change ≤ 3 percent, which is within the experimental error range. The achievement of coupling lengths less than 10 mm and the high synchronism of the guides suggest that these structures should be useful for electro-optic directional-coupler switches.

F. J. Leonberger
J. P. Donnelly
C. O. Bozler

C. BERYLLIUM-ION IMPLANTATION IN GaAs

We have previously reported the use of a multiple-energy Be^+ -ion implantation technique to create uniform-carrier concentration p-type layers in GaAs (see Ref. 9 in which we presented the carrier concentration vs depth of a GaAs layer implanted with $1.5 \times 10^{14} \text{ Be}^+/\text{cm}^2$ at 400 keV, $1.2 \times 10^{14} \text{ Be}^+/\text{cm}^2$ at 220 keV, and $1.2 \times 10^{14} \text{ Be}^+/\text{cm}^2$ at 100 keV). For this multiple-implanted sample, the measured p-type carrier concentration was found to be in good agreement with LSS theory.^{12,13} In this section, we report an extension of this work to higher total beryllium doses. In contrast to the results presented in Ref. 9 for a total dose of $3.9 \times 10^{14} \text{ cm}^{-2}$, significant diffusion of the implanted beryllium was observed for higher doses.

Details of the sample preparation, encapsulation, and anneal procedure can be found in Ref. 9. All the samples were implanted through a 700-Å encapsulating layer of pyrolytic Si_3N_4 (Refs. 14 and 15). The multiple beryllium doses used were $(5/13) N_T$ at 400 keV, $(4/13) N_T$ at 220 keV, and $(4/13) N_T$ at 100 keV, where N_T is the total ion dose. Except as noted,⁹ all the implants were made with the GaAs samples at room temperature. After implantation, the samples were annealed at 900°C for 15 min. Electrically isolated cloverleaf-shaped mesas were then defined in the implanted layer to minimize contact effects in making Hall measurements of the van der Pauw type.¹⁶

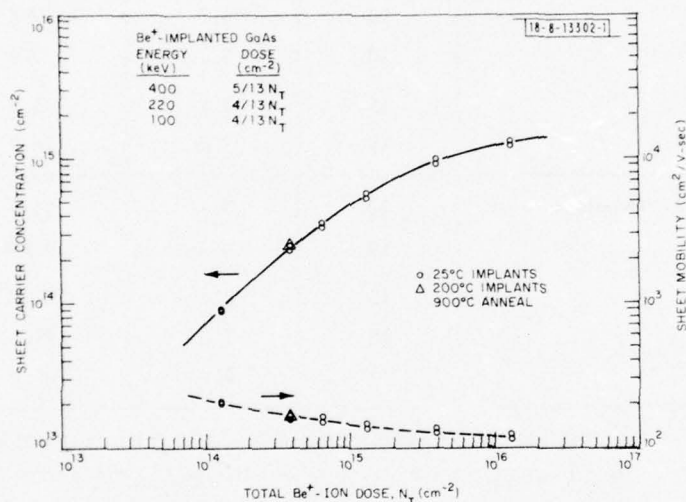


Fig. I-7. Sheet carrier concentration and mobility vs total ion dose for multiple Be^+ implants in GaAs. Implants were made through 700-Å Si_3N_4 encapsulation layer, and were chosen to give uniform carrier concentration.

Figure I-7 shows the measured sheet carrier concentration and mobility vs total Be-ion dose for several uniform-carrier-concentration implants. As the total dose increases, the ratio of the measured sheet carrier concentration to total ion dose decreases. The measured effective activation (sheet carrier concentration/total ion dose) of the implanted Be^+ is 70 percent

for a total dose of $1.3 \times 10^{14} \text{ cm}^{-2}$, and 10 percent for a total dose of $1.3 \times 10^{16} \text{ cm}^{-2}$. We believe that in this range of carrier concentration, this apparent decrease in activation is primarily due to the increased statistical occupation of the Be acceptor level.¹⁷ Although an accurate theoretical fit has not been obtained because of uncertainties in the beryllium acceptor level ionization energy, the degeneracy factor, and possible banding effects, it appears that even for the higher doses studied, most (if not all) of the implanted Be is on electrically active sites. As shown in Fig. I-7, the sheet mobility decreases from about $210 \text{ cm}^2/\text{V-sec}$ for a total ion dose of $1.3 \times 10^{14} \text{ cm}^{-2}$, to about $120 \text{ cm}^2/\text{V-sec}$ for a total ion dose of $1.3 \times 10^{16} \text{ cm}^{-2}$.

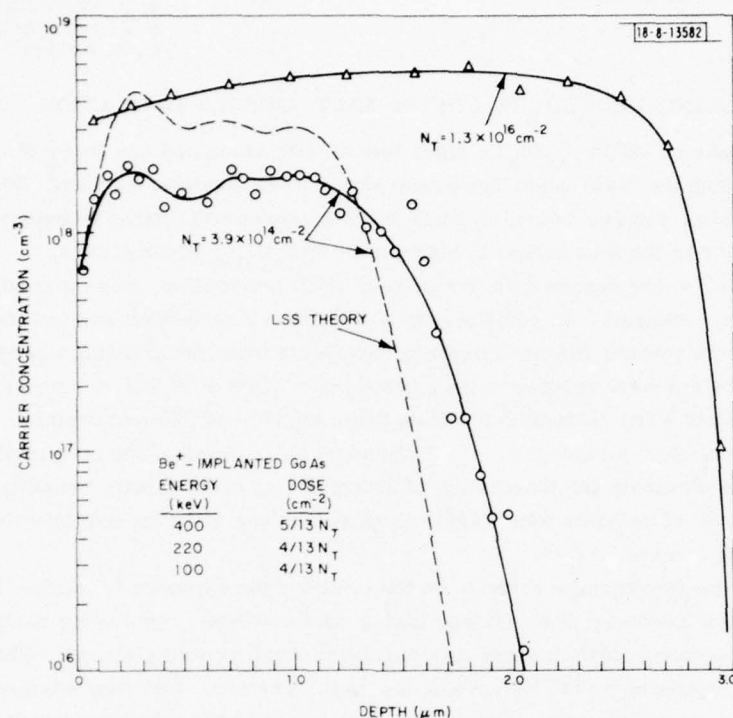


Fig. I-8. The p-type carrier concentration vs depth for two multiple Be⁺ implants in GaAs. Implants were made through a 700-Å Si₃N₄ encapsulation layer, and annealed at 900° C for 15 min. in flowing N₂.

Figure I-8 shows the carrier concentration vs depth of two GaAs samples: one was implanted with a total dose of $3.9 \times 10^{14} \text{ Be}^+/\text{cm}^2$ ($1.5 \times 10^{14} \text{ cm}^{-2}$ at 400 keV, $1.2 \times 10^{14} \text{ cm}^{-2}$ at 220 keV, and $1.2 \times 10^{14} \text{ cm}^{-2}$ at 100 keV); the other was implanted with a total dose of $1.3 \times 10^{16} \text{ Be}^+/\text{cm}^2$ ($5 \times 10^{15} \text{ cm}^{-2}$ at 400 keV, $4 \times 10^{15} \text{ cm}^{-2}$ at 220 keV, and $4 \times 10^{15} \text{ cm}^{-2}$ at 100 keV). These measurements were obtained from a series of etching steps and Hall measurements.^{14,18,19} The dashed line in Fig. I-8 corresponds to the calculated Be⁺ profile^{12,13} for the lower-dose implant ($N_T = 3.9 \times 10^{14} \text{ cm}^{-2}$). The measured profile for the lower-dose implant was previously presented in Ref. 9, where it is discussed in more detail. We present

it again here so that it can be compared more easily with the profile obtained for a high-dose implant ($N_T \approx 1.3 \times 10^{16} \text{ cm}^{-2}$). As can be seen, there is good agreement between the experimental data and the theoretical profile for the lower-dose implant. For the high-dose implant ($N_T = 1.3 \times 10^{16} \text{ cm}^{-2}$), however, the measured hole-concentration profile is much deeper than expected from LSS theory or from the results at the lower dose. As can be seen in Fig. I-8, the measured hole concentration was $\approx 5 \times 10^{18} \text{ cm}^{-2}$ (with variations from $4 \times 10^{18} \text{ cm}^{-2}$ to $6 \times 10^{18} \text{ cm}^{-2}$) to a depth of $2.7 \mu\text{m}$, at which point it decreased rapidly to an unmeasurable value. We believe that the increased depth for the high-dose implant is due to a Be concentration-dependent diffusion coefficient.

J. P. Donnelly
F. J. Leonberger
C. O. Bozler

D. IMPROVED DICING PROCEDURE FOR Pb-SALT LASER FABRICATION

The performance of DH $\text{Pb}_{1-x}\text{Sn}_x\text{Te}$ diode lasers with sides and end faces of the Fabry-Perot cavity cut using the high-speed Tempress saw²⁰ were reported earlier.³ We have investigated the level of work damage caused in PbTe by this convenient cutting technique, and have applied the technique in the fabrication of high-power $\text{PbS}_x\text{Se}_{1-x}$ diode lasers.

Pieces of PbTe, 4 mm square with surfaces of (100) orientation, were ground and etch-polished to 250- μm thickness. An additional 25 μm were removed from each surface by electro-polishing, in order to remove the work damage remaining from the grinding and etch-polishing steps. Pieces to be cut were mounted with beeswax on a slice of Si which, in turn, was mounted on a quartz flat. Cuts were made with a 38- μm blade on 380- or 500- μm centers, to duplicate the conditions under which stripe-geometry lasers are cut. Parts of the cut strips were diced to 760- μm length to duplicate the fabrication of Fabry-Perot cavities with sawed faces. The cut PbTe was cleaned of beeswax with warm trichloroethylene and then was given a dislocation etch to reveal work damage.

The extent of the saw damage depends on the cutting rate. Generally, a slow advance of the work under the blade produces less damage than a fast advance, and cutting thick material ($> 50 \mu\text{m}$) in steps produces less damage than cutting through in a single pass. The slowest advance speed normally found on the Tempress saw is 0.5 cm/sec. Our saw was purchased with an extra slow advance speed of 0.05 cm/sec. Figure I-9 shows the damage induced at the

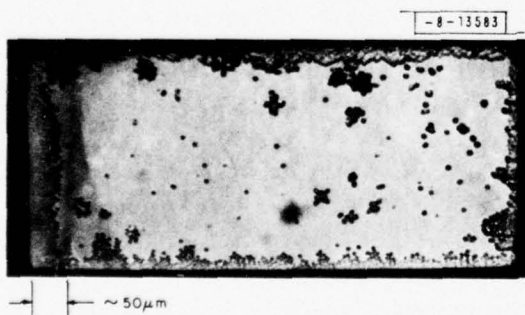


Fig. I-9. Photomicrograph of device-sized PbTe chip showing damage caused by four saw cuts. Individual etch pits inside border region are due to dislocations in bulk material, and groups of etch pits are due to work damage remaining from surface preparation.

intersection of a cut made perpendicular to two parallel cuts, similar to that produced in dicing laser chips. These cuts were made at a work advance speed of 0.05 cm/sec, cutting through the material 200 μm thick in steps of 25 μm per pass. The depth of damage is quite reproducible, extending about 50 μm from the cut edge. The individual etch pits seen inside that region are due to the dislocations in the bulk material, and the groups of etch pits are due to work damage remaining from the surface preparation. Additional saw damage may result, however, when cutting narrow strips. Figure I-10 shows damage extending across a 380- μm -wide strip of PbTe. This extended damage can be largely eliminated by providing support at the end of the strip with a block of PbTe or Si. This effect is also observed when cutting thin strips with the more commonly used wire-slurry saw. This study shows that the damage caused by cutting PbTe with the Tempress saw is uniform, and can be kept to within 50 μm of the cut edge. We have found this damage comparable to that of a wire-slurry saw, but the Tempress saw produces truer cuts and is considerably easier to use.

Fig. I-10. Photomicrograph of section of saw-cut strip of PbTe showing damage that results when end support is not given to PbTe during cutting.



The surfaces produced by cutting with the Tempress saw are sufficiently reflective to reproducibly obtain laser action when used as end faces of Fabry-Perot cavities of Pb-salt lasers. The quality of the sawed surface, however, does leave more damage than the best cleaved surface, which can be essentially damage-free away from the edge where the cleave is initiated. Good cleaves have not been reproducible, and the cleaving process frequently produces macroscopic damage such as cracks which may extend throughout the laser chips. Generally, the quality of the cleave improves as the thickness of the material decreases. On the other hand, it is difficult to handle slices of Pb-salt material less than 175 μm thick without causing damage.

A process involving sawing and cleaving combines the advantages of both techniques, and has been used to fabricate $\text{PbS}_{1-x}\text{Se}_x$ diode lasers of uniformly high quality. The objective is to reduce the thickness of the material only where the cleave is desired by cutting a groove with the saw. In the combined saw-cleave process, material of $\sim 200\text{-}\mu\text{m}$ thickness is sawed from the side away from the p-n junction to a depth of $\sim 100\text{ }\mu\text{m}$. This is thick enough so that the saw damage does not extend into the region of the p-n junction, but thin enough so that cleaves which are initiated in the saw groove have uniformly high quality. The saw grooves are made perpendicular to diffused stripes so that the cleaved surfaces form the end faces of the Fabry-Perot cavity. The saw is then used to cut apart the individual laser chips.

TABLE I-2 LASER CAVITIES FABRICATED BY CLEAVING							
Diode No.	Crystal No.	Anneal		Diffusion		I_t (mA)	CW Power (mW)
		Temperature (°C)	Time (days)	Temperature (°C)	Time (hr)		
2870	37.3 Se-32A	450	14	500	3	210	12
2871	37.3 Se-32A	500	7	500	3	590	2.7
3039	37.3 Se-32A	550	8	550	1	420	5
3046	37.3 Se-32A	550	8	550	1	570	10
2950	39 Se-109A	550	5	550	1	375	14
2962	39 Se-109A	550	5	550	1	590	3.5
2969	39 Se-109A	550	5	550	1	360	3.1
3003	39 Se-109A	550	5	550	1	210	6.3
3006	39 Se-109A	550	5	550	1	200	17

TABLE I-3 LASER CAVITIES FABRICATED BY SAWING AND CLEAVING							
Diode No.	Crystal No.	Anneal		Diffusion		I_t (mA)	CW Power (mW)
		Temperature (°C)	Time (days)	Temperature (°C)	Time (hr)		
3128	37.3 Se-32A	500	30	500	4	375	47.2
3130	37.3 Se-32A	500	30	500	4	320	55.7
3137	32.5 Se-88	500	5	500	4	188	≈ 50
3138	32.5 Se-88	500	5	500	4	320	53.0
3139	32.5 Se-88	600	5	500	4	545	≈ 50
3144	32.5 Se-88	600	5	500	4	250	≈ 40
3156	26.7 Se-89	575	5	500	4	550	≈ 40
3157	26.7 Se-89	575	5	500	4	390	≈ 20
3159	26.7 Se-89	575	5	500	4	450	≈ 50

Lists of parameters of several laser diodes with Fabry-Perot end faces formed by cleaving only, and by sawing and cleaving, are shown in Tables I-2 and I-3, respectively. The lists include several different n-type as-grown crystals which were annealed p-type in a SSe-rich atmosphere using different annealing parameters. Using MgF_2 as a diffusion barrier, 75- μm -wide n-type stripes were diffused in a Pb-rich atmosphere using the various diffusion parameters shown. All these laser cavities are approximately 400 μm long. Although the variation in lasing threshold currents (I_t) for these two groups of devices is comparable, the single-ended CW output power is significantly higher and more uniform for the devices using the combination of sawing and cleaving. Using different crystals or different annealing and diffusion parameters (in the ranges shown) seems to have little or no effect on the output powers.

The saw-cleave technique has considerably increased the output power and uniformity of $\text{PbS}_{1-x}\text{Se}_x$ lasers. Similar, but somewhat less conclusive, results were observed at lower power levels (≈ 1 mW) for $\text{Pb}_{1-x}\text{Sn}_x\text{Te}$ lasers.

J. M. Lawless
A. R. Calawa
S. H. Groves

REFERENCES

1. H. Kogelnik and C. V. Shank, J. Appl. Phys. 43, 2327 (1972).
2. H. C. Casey, Jr., S. Somekh, and M. Ilegems, Appl. Phys. Lett. 27, 142 (1975); M. Nakamura, K. Aiki, J. Umeda, and A. Yariv, Appl. Phys. Lett. 27, 403 (1975). These are two of the more recent references for this type of laser, and contain references to earlier work.
3. J. N. Walpole, A. R. Calawa, T. C. Harman, and S. H. Groves, Appl. Phys. Lett. 28, 552 (1976).
4. H. L. Garvin, E. Garmire, S. Somekh, H. Stoll, and A. Yariv, Appl. Opt. 12, 455 (1973).
5. R. W. Ralston, J. N. Walpole, T. C. Harman, and I. Melngailis, Appl. Phys. Lett. 26, 64 (1975), DDC AD-A007894/9.
6. H. F. Taylor and A. Yariv, Proc. IEEE 62, 1044 (1974).
7. F. J. Leonberger, J. P. Donnelly, and C. O. Bozler, Appl. Phys. Lett. 28, 616 (1976).
8. Solid State Research Report, Lincoln Laboratory, M.I.T. (1975:4), p. 1, DDC AD-A025489.
9. *Ibid.* (1976:1), p. 5.
10. J. P. Donnelly, F. J. Leonberger, and C. O. Bozler, Appl. Phys. Lett. 28, 706 (1976).
11. G. H. Olsen and M. Ettenberg, J. Appl. Phys. 45, 5112 (1974).
12. J. Lindhard, M. Scharff, and H. Schiott, K. Dan Vidensk. Selsk. Mat.-Fys. Medd. 33, 1 (1963).
13. W. J. Johnson and J. F. Gibbons, Projected Range Statistics in Semiconductors (Stanford University Bookstore, 1970).
14. J. P. Donnelly, W. T. Lindley, and C. E. Hurwitz, Appl. Phys. Lett. 27, 41 (1975), DDC AD-A016690/0.
15. Solid State Research Report, Lincoln Laboratory, M.I.T. (1975:1), p. 8, DDC AD-A009848/3.
16. L. J. van der Pauw, Philips Res. Rep. 13, 1 (1958).
17. J. F. Gibbons and R. E. Tremain, Jr., Appl. Phys. Lett. 26, 199 (1975).
18. J. D. Sansbury and J. F. Gibbons, Appl. Phys. Lett. 14, 311 (1969).
19. J. M. Woodcock, J. M. Shannon, and D. J. Clark, Solid-State Electron. 18, 267 (1975).
20. Sola-Basic Industries, Tempres Microelectronics Division, Los Gatos, California, Model 602 dicing saw.

II. QUANTUM ELECTRONICS

A. EFFICIENT HIGH REPETITION RATE PULSED SECOND-HARMONIC GENERATION IN CdGeAs_2

In order to improve the efficiency of doubling in CdGeAs_2 , the pulse output of the chopper-wheel Q-switched CO_2 laser¹ as well as second-harmonic output were studied as a function of pulse separation.

Since the period between pulses at high repetition rates is too short to permit maximum inversion buildup of the CO_2 molecules, a rapid reduction of laser pulse amplitude with increasing frequency at high prf occurs. This is illustrated by the dashed curve in Fig. II-1, which shows the relative CO_2 laser pulse amplitude P_A as a function of pulse separation under conditions of fixed electrical input to the laser and constant chopper wheel velocity. The prf variation was obtained by using wheels with different numbers of slots.

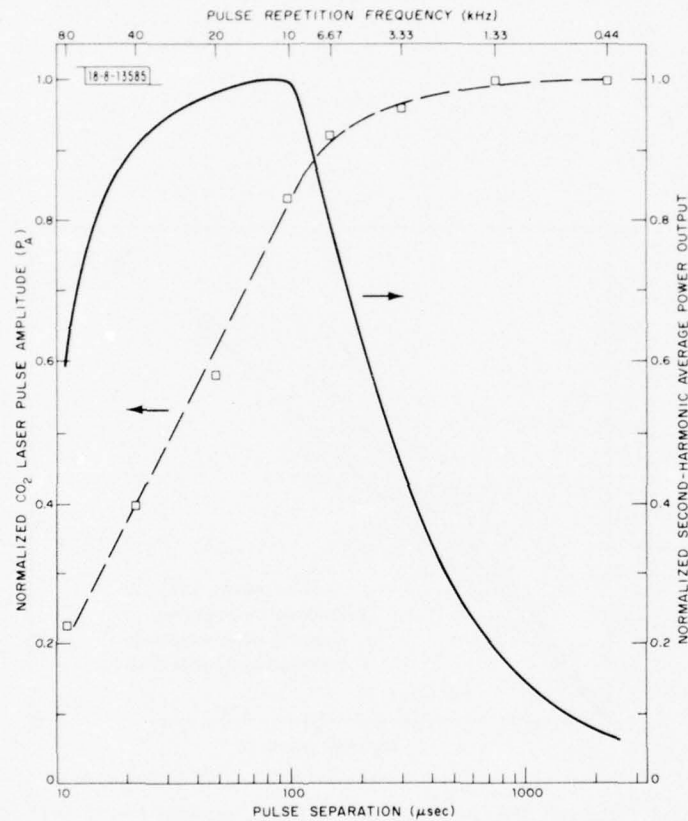


Fig. II-1. Dashed line: normalized variation of CO_2 laser pulse amplitude with pulse separation. Solid line: normalized variation of second-harmonic average power in CdGeAs_2 with pulse separation, based on dashed line and assumption $\langle P(2\omega) \rangle \propto \nu P_A^2$.

TABLE II-1 SHG OF Q-SWITCHED CO ₂ LASER RADIATION							
Wheel Slot No.	Pulse Rate (kHz)	Average Values			Peak Values		
		P(ω) (W)	P(2 ω) (W)	Percent Efficiency	P(ω) (W)	P(2 ω) (W)	Percent Efficiency
180	47.4	7.1	0.79	11.1	—	—	—
45	11.7	4.6	0.76	16.3	—	—	—
6	1.55	0.77	0.158	20.5	1840	560	30.4

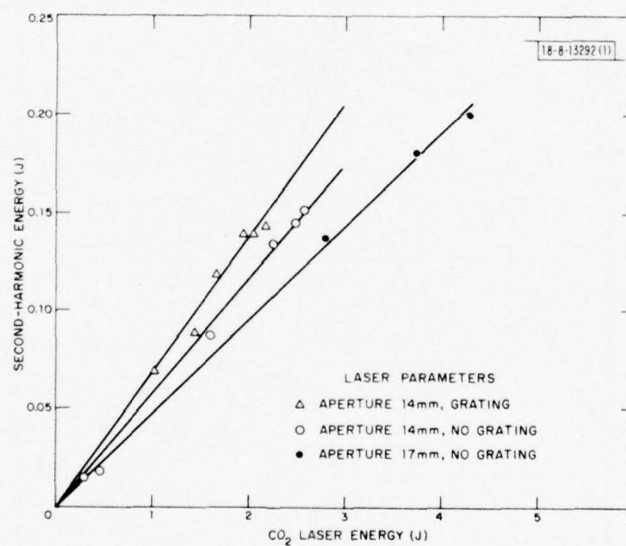


Fig. II-2. Pulsed SHG in uncoated CdGeAs₂ crystal $8 \times 12 \times 11 \text{ mm}^3$.

Since second-harmonic generation (SHG) is proportional to the square of the pump amplitude in the absence of saturation effects, the average second-harmonic output will be proportional to $\nu(P_A)^2$, where ν is the prf, and a constant pulse shape is assumed. The normalized average second-harmonic output, based on the P_A vs ν curve, is also shown in Fig. II-1 and indicates that the highest average outputs are available between about 8 and 50 kHz. The SHG output per pulse is proportional to P_A^2 . Therefore, while the average output decreases with decreasing prf below 10 kHz, SHG conversion efficiency will continue to increase.

The experimental SHG results broadly follow the behavior expected on the basis of Fig. II-1. However, there are differences in detail due to departures from the assumptions made in obtaining the curve. In particular, it was found that the CO_2 output level at low prf maximized at a lower electrical input to the laser than for a higher prf. This had the effect of skewing the curve to favor the higher prf levels.

The optimum SHG results obtained to date with this laser are shown in Table II-1. They represent an improvement over the results previously reported, due to a somewhat improved mode quality of the laser and, in the one case, to the use of a 6-slot wheel with a greater ratio of slot spacing to slot width. There was no sign of saturation in the waveform of the 5.3- μm second-harmonic output corresponding to the average and peak conversion efficiencies of 20.5 and 30.4 percent, respectively.

N. Menyuk
A. Mooradian
G. W. Iseler

B. HIGH PEAK POWER SECOND-HARMONIC GENERATION IN CdGeAs_2

We have obtained 0.2-J second-harmonic energy from an uncoated CdGeAs_2 crystal $8 \times 12 \times 11 \text{ mm}^3$. Figure II-2 shows the dependence of the second-harmonic output energy on the CO_2 laser energy incident on the doubling crystal. The relatively low second-harmonic conversion efficiencies of 5 to 7 percent in these experiments are due to the properties of the laser pulse which was multimode and had a tail because of nitrogen in the laser mixture. The linear slope is probably due to saturation caused by absorption in the crystal and the multimode character of the laser beam. It should be possible to increase the second-harmonic energy further to 0.5 J by antireflection-coating the crystal. The highest second-harmonic energies that have been reported by doubling CO_2 laser radiation in commercially available nonlinear materials such as proustite or tellurium are less than 1 mJ.

We have also experimented with antireflection-coated CdGeAs_2 crystals, and have observed an external energy conversion efficiency of 27 percent for a 12-mm-long crystal. This was obtained using a 70-nsec, TEM_{00} mode, CO_2 TEA laser pulse. We did not observe saturation effects similar to the unexplained effects that we reported previously for a 150-nsec pulse on an uncoated crystal. The measured conversion efficiency for the 12-mm-long crystal is in good agreement with calculations, assuming absorption constants of 0.2 and 1.5 cm^{-1} at the CO_2 and second-harmonic wavelength, respectively. With this absorption the crystal length is not optimum, however. We estimate from computer calculations that a 6-mm coated crystal should give a conversion efficiency of 40 percent, assuming that no other limiting effects are present except for losses due to linear absorption and pump depletion.

We measured the laser-induced surface damage threshold for antireflection-coated CdGeAs_2 samples. Compared with uncoated crystals, there is only a slight reduction of 10 to 20 percent in the threshold for pit and plasma formation. We also measured the pulse length dependence

of the damage threshold for pulse lengths between 70 and 150 nsec. The damage threshold depends only on the total energy per unit area for these pulse lengths.

H. Kildal
G. W. Iseler

C. THERMAL RUNAWAY IN CdGeAs₂

The critical power level for thermal runaway in CdGeAs₂ as a function of bath temperature has been calculated. The model used for the calculation is one in which a cylinder (sample) of radius R is irradiated by a laser beam of radius ρ , as indicated in Fig. II-3(a). The thermal contact is assumed imperfect, and is defined by a thermal contact parameter

$$h = - \frac{K}{[T_{\text{BATH}} - T(R)]} \left. \frac{\partial T(r)}{\partial r} \right|_{r=R}$$

where K is the thermal conductivity, T_{BATH} is the bath temperature, and $T(R)$ is the sample temperature at its perimeter. Therefore, $h = \infty$ corresponds to setting the sample perimeter at the bath temperature. For this model, it has been shown² that the critical power level for thermal runaway is

$$P_c = \frac{1}{S} \left(\frac{4\pi K}{1 + \frac{2K}{hR} + 2 \ln \frac{R}{\rho}} \right) \quad (\text{II-1})$$

In Eq. (II-1), S is a bath-temperature dependent quantity illustrated in Fig. II-3(b) for $T_{\text{BATH}} = 200$ K. It is the slope of a line which goes through the bath temperature at zero absorption and is tangent to the optical absorption coefficient curve.

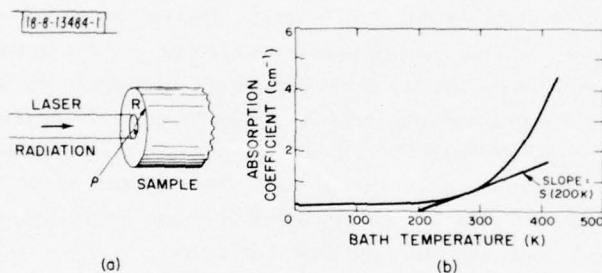
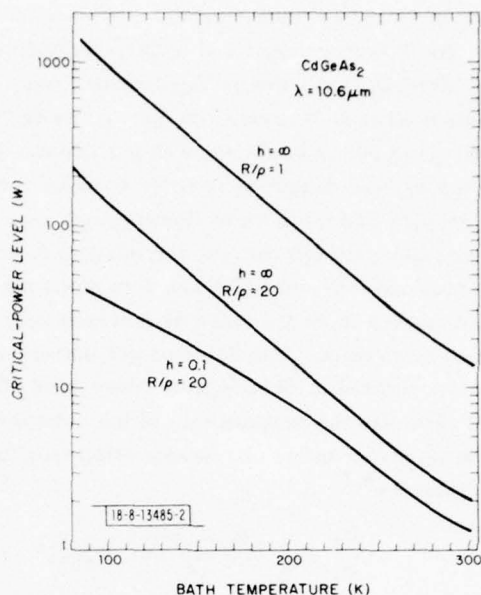


Fig. II-3. (a) Definition of R and ρ in thermal runaway model; (b) temperature variation of CdGeAs₂ absorption coefficient at 10.6 μm . Also illustrated is slope function S for bath temperature of 200 K.

The curve in Fig. II-3(b) is based on optical transmission measurements taken between 4.2 and 450 K on CdGeAs₂ sample No. 76-19B. Taking the $S(T)$ values from this curve, and using the K -vs- T values of Leroux-Hugon,³ the critical power level for thermal runaway as a function of bath temperature at 10.6 μm for different values of h and R/ρ are shown in Fig. II-4, with R taken equal to 2 mm. This value and $R/\rho = 20$ approximate the conditions of our focused-beam SHG experiments.

CdGeAs₂ can accept fairly high levels of CO₂ laser radiation with reasonable thermal contact to an 80 K bath temperature. However, the rapid decrease of P_c with increasing temperature indicates that safe and effective use of CdGeAs₂ requires that the crystal be cooled.

Fig.II-4. Variation of critical power level for thermal runaway with bath temperature for different values of R/ρ and thermal contact parameter h .



A similar calculation was carried out for a wavelength of $5.3 \mu\text{m}$. The higher optical absorption at this shorter wavelength leads to an approximately five-fold decrease in the value of P_c , and the temperature dependence is similar to the $10.6\text{-}\mu\text{m}$ case.

N. Menyuk
H. Kildal

D. INFRARED THIRD-HARMONIC GENERATION IN PHASEMATCHED CO GAS

Recently, third-harmonic generation (THG) of CO_2 laser radiation has been observed in SF_6 , BCl_3 , and CO (see Refs. 4 and 5). Both SF_6 and BCl_3 have strong absorption at the CO_2 pump wavelength, which limits the maximum obtainable third-harmonic conversion efficiency in these gases. This problem is avoided for CO which has only a two-photon resonance with the CO_2 pump laser, and there is a potential for scaling of the efficiency when phasematching techniques are employed. The CO itself, because of the vibrational resonance at 2143 cm^{-1} , has negative dispersion between the third harmonic and the CO_2 pump frequency. Phasematching is therefore possible if CO is mixed with a gas with positive dispersion. Similar phasematching techniques have previously been employed for atomic vapors in the visible and ultraviolet spectral regions.⁶

In this report, we discuss phasematched THG in CO using SF_6 gas to provide the necessary positive dispersion for phasematching. The measured third-order susceptibility for CO is in good agreement with calculations which relate the third-order susceptibility to the spontaneous Raman scattering cross section, and the measured difference in the indices of refraction between the third harmonic and the laser pump frequency is also in good agreement with predictions. We also report on THG in NO using a two-photon resonance between the CO_2 pump laser and the NO Q-branch, and the efficiency is about the same as for CO.

For the third-harmonic experiments we used a grating-controlled, TEM₀₀ mode, CO₂ TEA laser. The laser operated with a CO₂-He gas mixture; N₂ was omitted to avoid the tail on the output pulse caused by the energy transfer from N₂. The laser pulse had some structure due to spontaneous modelocking, and the width was 70 nsec (FWHM). The output from the laser, typically 50 to 200 mJ as measured with a Gen-Tec ED-200 joule meter, was passed through an 8- μ m long-wavelength-pass filter to block the third-harmonic signal generated in the Ge output coupler and the 4.3- μ m fluorescence from the CO₂ laser. The beam was then focused by a long-focal-length mirror into the third-harmonic cell which was equipped with a NaCl window in the front and a 5-mm LiF window to block the CO₂ laser radiation in the back. The third-harmonic output from the cell was detected with an InSb photovoltaic detector that had a time constant of 525 nsec. The detector did therefore not resolve the third-harmonic pulse, and this was corrected in determining conversion efficiencies. A He-Ne laser at 3.39 μ m was used to calibrate the responsivity of the detector.

The third-harmonic conversion efficiency for TEM₀₀ mode lasers when there is no absorption is given by^{4,7}

$$\frac{P_3}{P_1} = \frac{3}{4} \frac{\eta^4 \omega^2 |\chi^{(3)}|^2}{\lambda^2} P_1^2 |\mathcal{J}|^2 \quad (\text{II-2})$$

where the third-order susceptibility $\chi^{(3)}$ is defined by $\mathcal{P}_3 = \chi^{(3)} \mathcal{E}_1^3$, and \mathcal{E}_1 and \mathcal{P}_3 are the Fourier amplitudes of the applied electric field and the resulting polarization. The phase mismatch integral \mathcal{J} in Eq. (II-2) can be written as⁷

$$\mathcal{J} = \frac{2}{b} \int_0^l \frac{\exp \{i\Delta k z + i2 \arctan [2(z - z_0)/b]\}}{1 + [2(z - z_0)/b]^2} dz \quad (\text{II-3})$$

where $\Delta k = k_3 - 3k_1$ is the wavevector mismatch, l is the cell length, z_0 is the distance from the cell entrance window to the focal point, and $b = 2\pi w_0^2/\lambda$ is the confocal parameter where w_0 is the spot size of the laser beam at the focal plane. It follows from Eq. (II-3) that the phase change which occurs when the Gaussian beam propagates through the focal region can be compensated for, at least partially, by a negative wavevector mismatch when the beam is focused in the middle of the cell. $|\mathcal{J}|^2$ is maximized for $\Delta k/b$ values ranging from -2 at tight focusing ($b \ll l$) to -4 at weak focusing ($b \gg l$).

Figure II-5(a) shows the third-harmonic signal obtained from a 17.9-cm cell filled with CO-SF₆ mixtures at pressures up to 11 atm. The pump line is the CO₂ R(10) line at 1071.884 cm⁻¹. For pure CO, the third-harmonic signal vs pressure curve shows oscillations with amplitudes that decrease with increasing pressures. This is typical for negative Δk . By adding SF₆, the period of oscillations increases until the phasematching condition $\Delta k = 0$ is reached with a CO-SF₆ ratio of 1:0.0048. At higher SF₆ partial pressures, the oscillations appear again, but now the amplitude of the first oscillation is smaller than the successive amplitudes, as expected when Δk is positive.

The phase mismatch integral is pressure-independent at phasematching, and the pressure dependence of the third-harmonic signal is then determined by $|\chi^{(3)}|^2$ which is proportional to pressure squared as long as the effects of pressure broadening on $\chi^{(3)}$ are negligible. Experimentally, the pressure broadening begins to limit $\chi^{(3)}$ at pressures above a couple of atmospheres for the CO₂ R(10) line. We can estimate the third-order susceptibility for CO enhanced

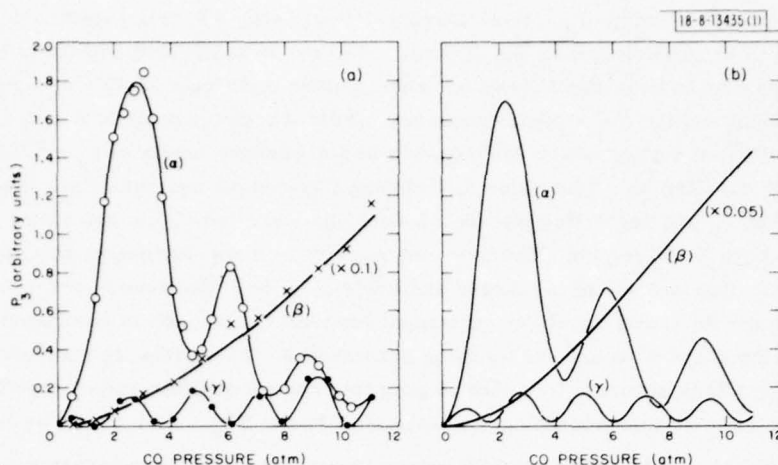


Fig. II-5. Pressure dependence of third-harmonic signal from 17.9-cm cell filled with CO-SF₆ mixtures of (α) 1:0, (β) 1:0.0048, and (γ) 1:0.012, and pumped with CO₂ R(10) line at 9.33 μm focused at cell exit window. (a) Measured signal, (b) calculated signal.

by the two-photon resonance between the pump laser and the CO 0 → 1 Q-branch using the expression⁴

$$\chi^{(3)} \approx \frac{8\pi^2}{\mu_0 \hbar} \frac{(d\sigma^r/d\Omega)}{\omega_r \omega_s^3} \sum_J \frac{N_J}{\omega_{Q(J)} - 2\omega - i\Delta\omega_{Q(J)}/2} \quad (\text{II-4})$$

where J is the rotational quantum number, $\omega_{Q(J)}$ and $\Delta\omega_{Q(J)}$ are the frequencies and linewidths of the Q-branch transitions, ω is the laser frequency, N_J is the density of molecules in a single rotational level of the vibrational ground state, $d\sigma^r/d\Omega$ is the Q-branch vibrational Raman scattering cross section with incident and scattered light polarized in the same direction, and ω_r and ω_s are, respectively, the Raman pump and Stokes frequency. The Raman scattering cross section for the Q-branch is slightly J -dependent. The variation with J , however, which is only a few percent, has been neglected in Eq. (II-4) such that measured cross sections for the total Q-branch can be used directly. In Eq. (II-4), we are also assuming that the main contribution to $\chi^{(3)}$ from intermediate states comes from the summation over excited electronic states, except for the vibrational two-photon resonance.⁴ Furthermore, it is assumed that ω_r is sufficiently below the electronic transition frequencies such that there is no electronic resonance enhancement of $d\sigma^r/d\Omega$.

In calculating $\chi^{(3)}$ for CO, we use $d\sigma^r/d\Omega = 4.3 \times 10^{-31} \text{ cm}^2 \text{ sr}^{-1} (\lambda_r = 5145 \text{ Å})$ (see Ref. 8), and $N_J = N(2J+1) \exp[-\hbar B J(J+1)/kT]$, where $B/2\pi c = 1.93 \text{ cm}^{-1}$ is the rotational constant, and $N = 2.49 \times 10^{25} \text{ m}^{-3} \text{ atm}^{-1}$ at 22°C. The frequencies for the Q-branch are obtained from the molecular constants in Ref. 9, and the linewidths for the individual J lines, which are determined by pressure broadening above a few tens of Torr, are taken from Ref. 10. (We assume that the pressure broadening for the Q-branch is similar to the R-branch. It should depend mainly on the rotational quantum number J .)

Figure II-5(b) shows the calculated pressure dependence of the third-harmonic signal for three CO-SF₆ mixtures in Fig. II-5(a), assuming the same input power in each case. The

calculations were made using Eqs. (II-2) through (II-4), with the cell length and focusing parameters as in the experiment in Fig. II-5(a). In order to evaluate the phase mismatch integral, it is necessary to know the difference in the indices of refraction $\delta n = n_3 - n_1$ between the third harmonic and the laser pump frequency. For CO, pumped with the CO₂ R(10) line, $\delta n_{\text{CO}} = -5.2 \times 10^{-6}$ at 1 atm, which corresponds to a coherence length of $l_c = \pi/|\Delta k| = \lambda/6|\delta n_{\text{CO}}| = 30$ cm (Ref. 4). This value was obtained by considering only the vibrational resonance at 2143 cm⁻¹, and neglecting the contribution from excited electronic states to the dispersion in the 3- to 9- μ m region. The error because of this approximation should be only a few percent. Comparison of the measured and calculated third-harmonic curves for pure CO in Figs. II-5(a) and (b) shows excellent agreement between the periods of oscillation which are determined by the dispersion and the focusing parameters. From this we conclude that the calculated δn for CO is accurate to within 10 percent, and we use this value, together with the CO-SF₆ mixing ratio at phasematching, to determine δn for SF₆. At 1 Torr, we have $\delta n_{\text{SF}_6} = 1.43 \times 10^{-6}$. The δn values for CO and SF₆ given above were used in calculating the third-harmonic curve for the CO-SF₆ ratio of 1:0.012 in Fig. II-5(b). In this case, the coherence length is $l_c = 20$ cm at 1 atm. There is good agreement between the measured and calculated curves in Figs. II-5(a) and (b). The only disagreement is that the measured increase in signal amplitude under phasematched conditions is only half of what is predicted by the calculations.

The indices-of-refraction difference δn for SF₆ can also be estimated from the strength of the absorption band at 946 cm⁻¹. This absorption occurs on the low-frequency side of the pump laser, and therefore makes δn positive. Starting with Eq. (7) in Ref. 4, we obtain

$$\delta n = \frac{N|\mu_{10}|^2 \omega_{10}}{\epsilon_0 n_1} \left(\frac{1}{\omega_{10}^2 - (3\omega)^2} - \frac{1}{\omega_{10}^2 - \omega^2} \right) \quad (\text{II-5})$$

where the first term is the change in the index of refraction at the third-harmonic frequency, and the second term is the change at the pump frequency. Inserting the dipole moment $\mu_{10} = 0.3$ D (Ref. 11) and $\omega_{10}/2\pi c = 946$ cm⁻¹ for SF₆ into Eq. (II-5), together with $\omega/2\pi c = 1071.9$ cm⁻¹ for the CO₂ R(10) line, we find $\delta n = 6.7 \times 10^{-7}$ at 1 Torr, which is about half the measured value.

In addition to the CO₂ R(10) line, we have also observed THG of the CO₂ R(8), R(12), and R(14) lines. The doubled R(8) line falls in the middle of the CO Q-branch,⁴ and the doubled R(12) and R(14) are on the high-frequency side and further away from the Q-branch than the doubled R(10) line. At pressures below 1 atm, $\chi^{(3)}$ for R(12) and R(14) is therefore much smaller than for R(10). The difference is smaller at higher pressures, however, since the pressure broadening affects the R(10) pump line first. Figure II-6(a) shows the measured third-harmonic signal under phasematched conditions for the CO₂ R(8), R(10), R(12), and R(14) lines. At phasematching, the pressure dependence of the third-harmonic signal is determined by $|\chi^{(3)}|^2$, and in Fig. II-6(b) we show the calculated $|\chi^{(3)}|^2$ for the same four pump lines. The finite laser linewidth of approximately 0.03 cm⁻¹ has been neglected. This is important only for the R(8) line. The doubled R(8) line is within 0.036 cm⁻¹ of the CO 0 \rightarrow 1 Q(11) transition, and a finite linewidth reduces $|\chi^{(3)}|^2$ slightly at pressures below a couple of atmospheres. It is seen by comparing the figures that there is good qualitative agreement between the experiment and the calculation.

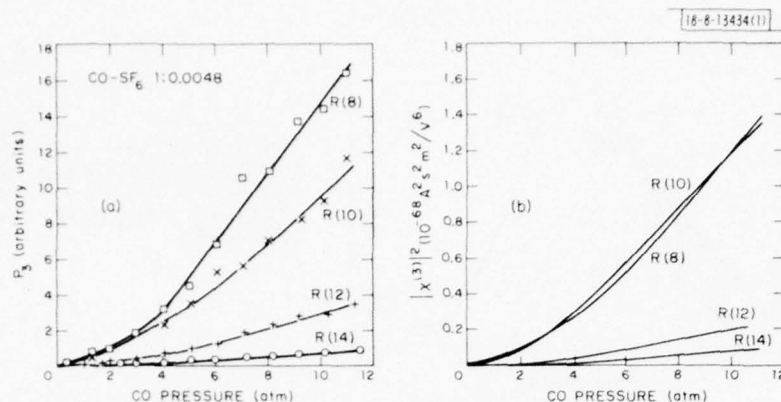


Fig. II-6. Pressure dependence of (a) third-harmonic signal generated in phasematched CO-SF₆ mixture pumped with CO₂ laser lines near 9.3 μ m, and (b) calculated third-order susceptibility squared for CO for same laser lines as in (a).

We have not observed any third-harmonic signal when utilizing a two-photon resonance between the CO₂ laser and the CO O-branch. In this case, only a single vibrational-rotational line contributes to the third-order susceptibility. This is different from the Q-branch, where the lines are narrowly spaced and the whole branch contributes to $\chi^{(3)}$.

The measured absolute third-harmonic conversion efficiency agrees well with theory. In a carefully calibrated experiment using the CO₂ R(10) line incident on a 32.7-cm cell filled with 700 Torr of CO, the measured third-harmonic power was $P_3 = 5.0 \times 10^{-3}$ W for an incident power of $P_1 = 1.3$ MW. This corresponds to a conversion efficiency of $P_3/P_1 = 3.8 \times 10^{-9}$. (The laser pulse in these experiments had some spontaneous modelocking. The degree, however, varied from pulse to pulse, and in taking measurements we only considered the pulses that had negligible modelocking.) At 700 Torr CO, the calculated third-order susceptibility from Eq. (II-4) is $|\chi^{(3)}| = 1.35 \times 10^{-35}$ Asm/V³. With a confocal parameter of $b = 32.8$ cm, $z_0 = 16.4$ cm, and a CO coherence length at 700 Torr of $l_c = \pi/|\Delta k| = 32.6$ cm, the phase mismatch integral in Eq. (II-3) is $|\int|^2 = 2.43$. With the above values inserted into Eq. (II-2) together with $P_1 = 1.3$ MW and $\omega/2\pi c = 1071.88$ cm⁻¹, we obtain $P_3 = 6.9 \times 10^{-3}$ W in good agreement with the observed value. This confirms that Eq. (II-4) is valid for calculating the third-order susceptibility when there is a resonance enhancement due to a vibrational two-photon transition.

We have also observed THG in NO with the same efficiency as in pure CO. The largest signal was obtained for the CO₂ P(28) line at 936.804 cm⁻¹. Using the CO₂ P(26) line, the signal was an order of magnitude smaller. The doubled P(28) line falls in the middle of the NO Q-branch, while the doubled P(26) is on the high-frequency side of the Q-branch. Figure II-7 shows the pressure dependence of the third-harmonic signal from CO and NO with the same input power in both cases. The NO has, as expected, a somewhat longer coherence length than CO since the vibrational dipole moment for NO is only 0.076 D (Ref. 12), compared with 0.1 D for CO (Ref. 13).

In Ref. 4 it was shown that the third-order susceptibility enhanced by a two-photon resonance is proportional to the two-photon absorption constant for that resonance. Therefore implicit in the THG experiments there is information about the strength of two-photon transitions.

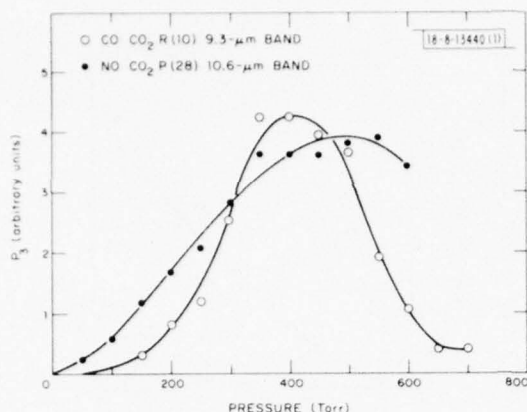


Fig. II-7. Pressure dependence of third-harmonic signal generated in CO and NO in 1-m cell with laser input power same in both cases.

A detailed calculation of the vibrational two-photon absorption constant for NO has been presented by Golger and Letokhov.¹⁴ As intermediate states, they consider only vibrational-rotational levels within the NO electronic ground state, neglecting contributions from excited electronic states. According to their calculations, the maximum two-photon absorption constant for the P and R branches is two orders of magnitude greater than for the S-, Q-, and O-branches. To examine this, we measured the third-harmonic signal generated using the CO₂ P(24) line at 940.549 cm^{-1} which is resonant with the NO R(0.5) transition in the $^2\pi_{1/2}$ state at 1881.041 cm^{-1} . (This is the same transition considered by Golger and Letokhov.) The larger two-photon absorption constant for the R-transition should more than compensate for the larger number of resonant lines in the Q-branch, to give a larger third-order susceptibility for the P(24) than for the P(28) line. Experimentally, however, this is not observed. The third-harmonic signal for the P(28) line is about 40 times larger than for the P(24) line. We believe that the model of Golger and Letokhov is incomplete. The excited electronic states, which were neglected by them, give the largest contribution to the two-photon absorption constant. For example, the two-photon absorption constants estimated from the spontaneous Raman scattering cross sections,^{4,15} which include the excited electronic states, are larger than the two-photon absorption constants calculated by Golger and Letokhov.

The largest third-harmonic conversion efficiency we have measured is 1.9×10^{-8} which was obtained for the CO₂ R(10) line with 1.2 MW of laser power incident on a 17.9-cm cell filled with a phasematched CO-SF₆ mixture at 11 atm. The energy density on the NaCl window in this experiment was 10 J/cm^2 . For a given cell length the conversion efficiency is limited by the damage threshold of the cell windows for confocal and weaker focusing, and by the optical breakdown of the gas for tight focusing.

With presently available lasers, it appears possible to scale up the THG efficiency in CO to reasonable levels. We consider a CO₂ laser operating on the R(8) transition, with an output pulse of 1 nsec and confocally focused into a cell filled with a CO-SF₆ mixture at 760 Torr. The CO-SF₆ ratio is set to maximize $|d|^2$; at confocal focusing this requires $\Delta kb = -3.46$, giving $|d|^2 = 2.46$. In this case, the predicted third-harmonic conversion efficiency is 10 percent for an input power of $P_1 = 3.4\text{ GW}$. When the energy density is limited by the NaCl window damage threshold¹⁶ for 1-nsec pulses of 6 J/cm^2 (energy density on the beam axis), and the experiment is performed at an energy density of half the damage threshold, a cell length of 24 m is necessary

to achieve the 10-percent conversion efficiency. The measured absorption in SF_6 over this path length is negligible.

H. Kildal

E. DIRECT OPTICALLY PUMPED MULTIWAVELENGTH CO_2 LASER

We report generation of laser radiation in the 16- to 17- μm region by optically pumping various isotopes of CO_2 using an HF laser. These experiments use a single HF laser to directly pump CO_2 . Our results indicate that efficient, tunable laser oscillation can be obtained and scaled to high-power levels. Numerous lines in the 4.3- μm region have also been generated. These play an important role in the overall system dynamics, as described below.

The experiments used either commercial HF lasers or oscillator amplifier systems. The cavities and optics were similar to those discussed in Ref. 17. However, in this case, the laser cells could be cooled to dry-ice temperature using concentric cooling jackets.

Four CO_2 species were pumped — $^{12}\text{C}^{16}\text{O}_2$, $^{12}\text{C}^{18}\text{O}_2$, $^{12}\text{C}^{16}\text{O}^{18}\text{O}$, and $^{13}\text{C}^{16}\text{O}^{18}\text{O}$. While all emitted in both the 4.3- and 10.6- μm range, $^{12}\text{C}^{18}\text{O}_2$ and $^{12}\text{C}^{16}\text{O}^{18}\text{O}$ also lased in the 17- μm region. The $\text{C}^{16}\text{O}^{18}\text{O}$ was available only in a mixture of $^{12}\text{C}^{18}\text{O}_2$: $^{12}\text{C}^{16}\text{O}^{18}\text{O}$: $^{12}\text{C}^{16}\text{O}_2$ with relative abundance ratios 1:2:1. Similar characteristics were observed from the C^{18}O_2 in the mixture and from a sample of 99-percent purity.

Comparisons of the known frequencies¹⁸ of HF lines with CO_2 absorption spectra in the 2.8- μm region^{19,20} reveal that $P_2 5$ (3577.500 cm^{-1}) is within 0.004 cm^{-1} of R8 from the $00^0_0 \rightarrow [10^0_1]_{\text{II}}$ † transition in $^{12}\text{C}^{16}\text{O}^{18}\text{O}$, and $P_2 6$ (3531.175 cm^{-1}) is within 0.007 cm^{-1} of R8 from the $00^0_0 \rightarrow [10^0_1]_{\text{II}}$ transition in $^{12}\text{C}^{18}\text{O}_2$. We verified these near coincidences and their absorption intensities by recording the transmission of the multiline HF laser spectrum with and without the $^{12}\text{C}^{16}\text{O}^{18}\text{O}$ mixture in the cell.

Using available spectroscopic constants,²¹ we have identified all the observed optically pumped output laser lines at 4.3 and 17 μm , and we list their calculated values in Table II-2. Our measurements were made using 0.5- and 1.0-m scanning monochromators, and the experimental numbers coincide to at least four significant figures with the calculated ones. The sole exception was the 16.76- μm line from $^{12}\text{C}^{16}\text{O}^{18}\text{O}$. This discrepancy was attributed to small deviations in the published constants, and in this instance the experimental number is also noted.

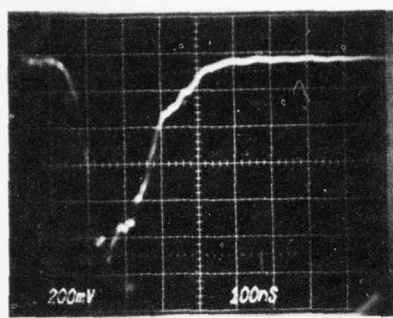
All 4.3- and 17- μm lines observed in these experiments can be accounted for by four populating processes: (1) 4.3- and 17- μm lines originating from the optically pumped levels, (2) 17- μm lines cascading from 4.3- μm lasing, (3) 4.3- μm lines pumped by rotational relaxation in $[10^0_1]_{\text{II}}$, and (4) 17- μm lines originating from rotational equilibration in $[10^0_0]_{\text{II}}$. This latter effect was much more pronounced with pure $^{12}\text{C}^{18}\text{O}_2$ than with either isotope in the mixture. The 10.6- μm lasing is due to fast V-V processes of the type (Ref. 22) $\text{CO}_2(021) + \text{CO}_2(000) \rightarrow \text{CO}_2(001) + \text{CO}_2(020)$, and was typically delayed from the pump pulse by several microseconds.

The temporal behavior of the laser pulses is illustrated in Fig. II-8(a-d), which shows the HF laser pulse, two 17- μm laser pulses from $^{12}\text{C}^{18}\text{O}_2$, and the 4.3- μm ($^{12}\text{C}^{18}\text{O}_2$) signal. There is ~50-nsec delay between the HF laser pulse and the directly pumped 17.46- and 4.3- μm lines. The weaker 17- μm lines in the cascade are further delayed relative to these lines by about 100 nsec.

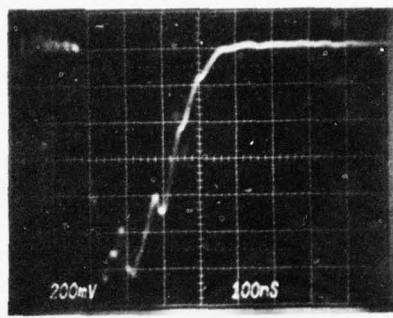
†We use the notation in which one Fermi resonant level is given in brackets, and the subscripts I, II, etc. indicate the particular level in order of decreasing energy.

TABLE II-2
CALCULATED VALUES OF OBSERVED LINES

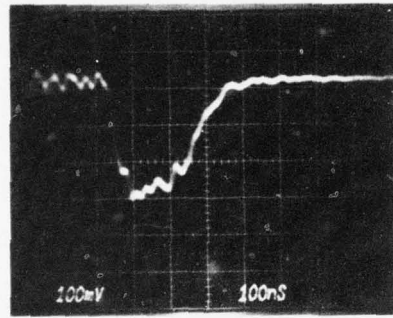
$^{12}\text{C}^{16}\text{O}^{18}\text{O}$ [pumped by $P_2(5)$]		$^{12}\text{C}^{18}\text{O}^{18}\text{O}$ [pumped by $P_2(6)$]	
		$[101]_{\parallel} \rightarrow 011$	
R(8)		16.780 μm (16.76)	R(8) 17.463 μm
		$[100]_{\parallel} \rightarrow 010$	
R(6)	16.596		R(7) 17.280
P9	16.927		P(7) 17.596
P11	16.970		P(9) 17.639
			P(11) 17.684
			P(13) 17.730
			P(15) 17.775
			P(17) 17.821
			P(21) 17.915
			P(23) 17.962
			P(25) 18.010
			P(27) 18.058
		$[101]_{\parallel} \rightarrow [100]_{\parallel}$	
R(8)	4.314		R(8) 4.346
P(10)	4.340		P(10) 4.371
P(14)	4.346		P(14) 4.377
P(19)	4.354		P(18) 4.382
			P(20) 4.385
			P(24) 4.392
			P(28) 4.398



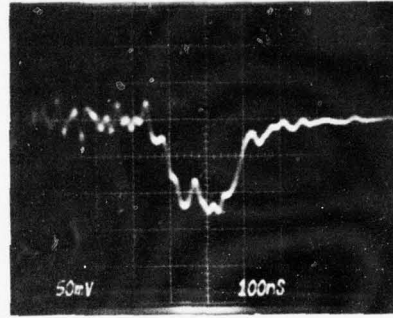
(a)



(b)



(c)



(d)

Fig. II-8. Laser pulses observed with 1-Torr $^{12}\text{C}^{18}\text{O}_2$: (a) P_{26} HF laser excitation pulse, (b) CO_2 laser emission pulse on $[10^0 1]_{\text{II}} \rightarrow [10^0 0]_{\text{II}}$ R8 transition at $4.346 \mu\text{m}$, (c) $[10^0 1]_{\text{II}} \rightarrow [01^1 1]_{\text{I}}$ R8 transition at $17.46 \mu\text{m}$, and (d) $[10^0 0]_{\text{II}} \rightarrow [01^1 1]_{\text{I}}$ P11 cascade line at $17.68 \mu\text{m}$.

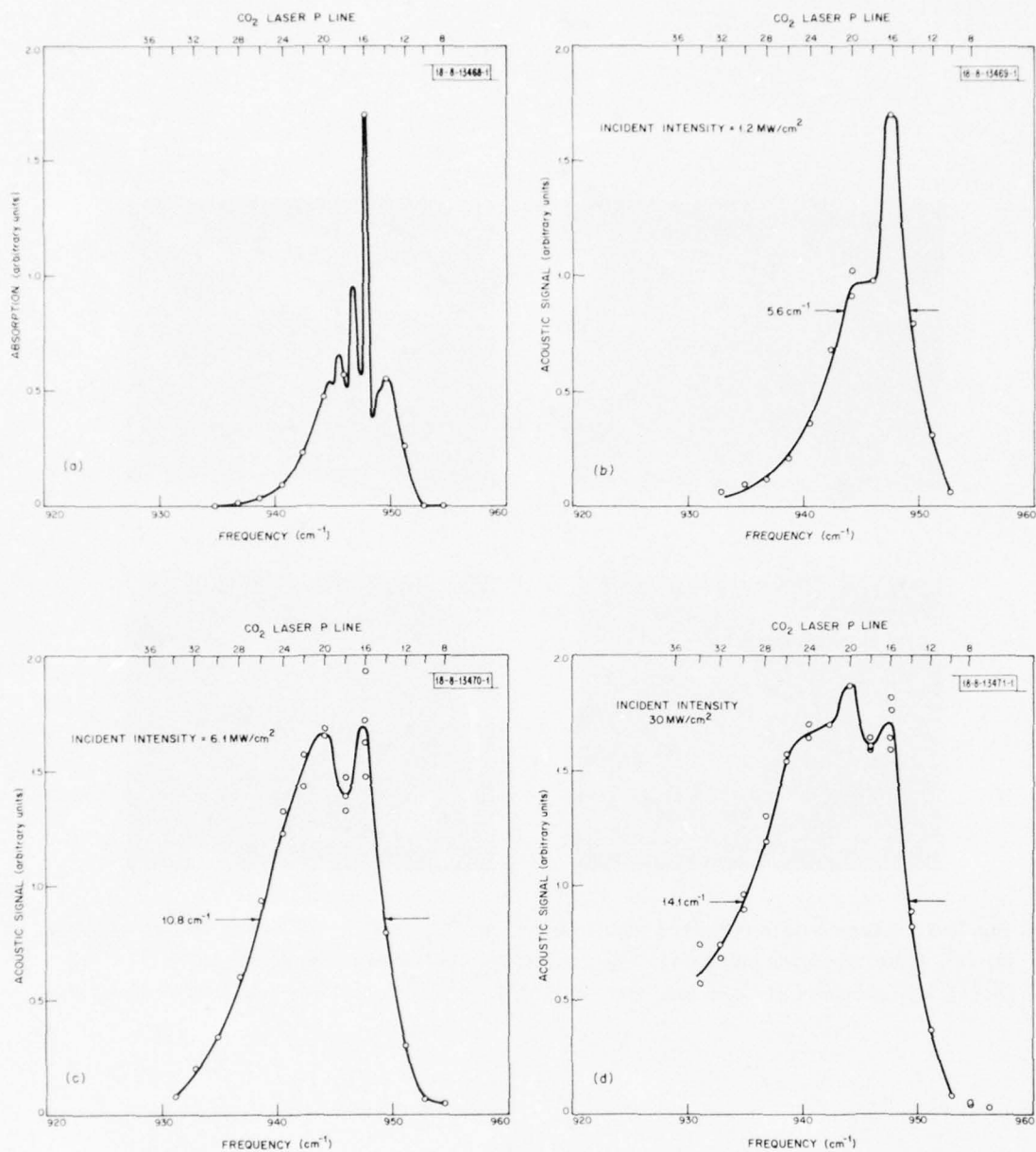


Fig. II-9. Absorption spectrum of 0.25 Torr SF_6 at 208 K (a) as measured with grating monochromator, and (b) through (d) obtained using CO_2 TEA laser and microphone. Points indicate absorption at CO_2 laser frequencies.

In summary, we have obtained new laser lines from 4.3- and 17- μm bands in two isotopes of CO_2 by direct optical pumping with a HF laser. Radiation at 4.3 μm was also seen in two additional isotopes. Considering the mechanisms involved, it is expected that these isotopes can also be made to oscillate at $\sim 16 \mu\text{m}$. We have demonstrated that rotational relaxation leads to many lines within 4.3- and 17- μm bands, and in our experiments have approached a condition of saturating the entire $00^0_0 \rightarrow [10^0_1]_{\text{II}}$ band.

M. I. Buchwald[†] H. R. Fetterman
C. R. Jones[†] H. R. Schlossberg[‡]

F. MULTIPHOTON ABSORPTION PROCESSES IN POLYATOMIC MOLECULES

Recent demonstrations of laser isotope separation in polyatomic molecules have been based on the selective dissociation of these molecules by a CO_2 laser.^{23,24} This dissociation can occur without collisions, indicating that a large number of infrared photons must be absorbed by each molecule. It has been suggested that the dissociation occurs in two steps, the first step being selective excitation to a vibrational state high enough that the density of states between it and the dissociation limit is essentially continuous.²⁵ The second step involves the nonselective absorption of enough infrared photons to dissociate the molecule. The first step is expected to show resonances at frequencies corresponding to the absorption of one, two, or three photons.²⁵

The dissociation of the SF_6 molecule has been studied extensively. We have extended the acoustic spectrophone technique, previously used on a CW basis, to the pulsed regime and have used it to measure the deposition of energy in SF_6 by a CO_2 TEA laser as a function of intensity and laser frequency.

The CO_2 TEA laser was a grating tuned unit, producing 100-mJ, multimode pulses at a rate of 4 Hz. The laser frequency could be varied from $P(8)$ to $P(34)$ of the 10.6- μm band; the pulse energy was kept constant as the frequency was varied by adding or removing attenuators placed in the beam. The beam was focused into the center of a 9-cm-long \times 19-mm-i.d. pyrex cell having NaCl windows by a 65-cm focal-length lens. The measured spot size at the focus was 1 mm. The central 6 cm of the cell had a cooling jacket; when cooled by a circulating dry ice and methanol mixture, the temperature at the center of the cell was measured to be 208 K. An electret condenser microphone was suspended at the center line of the cell. When the cell was filled with 1 Torr or less of SF_6 and the CO_2 laser beam was incident on the cell, an output pulse approximately 1 msec long was observed from the microphone. The signal disappeared when the cell was evacuated. The acoustic pulse is due to a pressure rise caused by the heating of the SF_6 gas when it absorbs energy from the beam; the pulse decays as the gas thermalizes with the cell walls. Acoustic resonances of the cell superimposed high-frequency oscillations on the pulse. The energy absorbed by the gas is proportional to the acoustic pulse amplitude, and so the absorption spectrum of SF_6 could be measured on a point-by-point basis using the CO_2 laser at various constant levels of energy.

Figure II-9(a) shows the absorption spectrum of 0.25 Torr SF_6 at 208 K as measured with a Spex 0.75-m double monochromator. The points indicate the location of the CO_2 laser lines and show how the structure would be distorted by a point-by-point laser measurement.

[†] Los Alamos Scientific Laboratory, Los Alamos, NM.

[‡] Rome Air Development Center, Hanscom AFB, MA.

Figures II-9(b), (c), and (d) show the acoustic signal vs frequency for 0.25 Torr SF_6 in the same cell with incident intensities of 1.2, 6.1, and 30 MW/cm^2 , respectively. In Fig. II-9(b), the spectrum is similar to what would be obtained by connecting the points corresponding to CO_2 laser frequencies in Fig. II-9(a). As the incident intensity increases, the absorption on the low-frequency side of the main absorption peak increases and a second absorption peak appears. This second peak, as well as the increased absorption on the red side, is believed to be due to multiphoton excitation of higher lying levels of the ν_3 mode of SF_6 .

For an anharmonic oscillator, the energy levels $G(v_3)$ are given by

$$G(v_3) = \omega_3 v_3 + X_{33} v_3^2 \quad (\text{II-6})$$

where v_3 is the vibrational quantum number for the ω_3 normal mode, and X_{33} is the anharmonicity constant. The zero-point energy has been set to zero. Nearly resonant excitation to $v = 1, 2, 3, \dots$ levels by multiphoton processes requires compensation of the anharmonic defect X_{33} ; this can be accomplished by differences in the rotational energy of the various transitions involved. One can interpret the peak at P(20) observed at high intensities as due to either a two-photon process involving a P and a Q transition, or a three-photon process involving P, Q, and R transitions. In either case, the separation between the peaks can be shown to be $2 X_{33}$. This interpretation allows the anharmonicity X_{33} of SF_6 to be estimated as -1.8 cm^{-1} . This value is in good agreement with the results of our spectroscopic measurements on SF_6 , which yield $X_{33} = -1.83 \text{ cm}^{-1}$.

T. F. Deutsch
P. F. Moulton

REFERENCES

1. Solid State Research Report, Lincoln Laboratory, M.I.T. (1976:1), p.30.
2. F. A. Horrigan and R. I. Rudko, "Materials for High-Power CO₂ Lasers," Final Technical Report, Raytheon Research Division, Contract No. DA-AH01-69-C-0038 (1969).
3. P. Leroux-Hugon, C. R. Acad. Sci. (Paris) 256, 3991 (1963).
4. H. Kildal and T. F. Deutsch, IEEE J. Quantum Electron. QE-12, 429 (1976).
5. M. H. Kang, K. M. Chung, and M. F. Becker, personal communication.
6. J. F. Young, G. C. Bjorklund, A. H. Kung, R. B. Miles, and S. E. Harris, Phys. Rev. Lett. 27, 1551 (1971).
7. J. F. Ward and G. H. C. New, Phys. Rev. 185, 57 (1969).
8. C. M. Penney, L. M. Goldman, and M. Lapp, Nature Phys. Sci. 235, 110 (1972).
9. H. Kildal, R. S. Eng, and A. H. M. Ross, J. Mol. Spectrosc. 53, 479 (1974), DDC AD-A006706/6.
10. G. M. Hoover and D. Williams, J. Opt. Soc. Am. 59, 28 (1969).
11. J. I. Steinfeld, I. Burak, D. G. Sutton, and A. V. Nowak, J. Chem. Phys. 52, 5421 (1970).
12. G. Chandraiah and C. W. Cho, J. Mol. Spectrosc. 47, 134 (1973).
13. S. S. Penner, Quantitative Molecular Spectroscopy and Gas Emissivities (Addison Wesley, Reading, Massachusetts, 1959).
14. A. L. Golger and V. S. Letokhov, Sov. J. Quant. Electron. 4, 478 (1974).
15. P. L. Kelley, H. Kildal, and H. R. Schlossberg, Chem. Phys. Lett. 27, 62 (1974), DDC AD-A002778/9.
16. W. H. Reichelt and E. E. Stark, Jr., Laser Induced Damage in Optical Materials: 1973, edited by A. J. Glass and A. H. Guenther (NBS Special Publication 387, December 1973), pp. 175-180.
17. W. E. Barch, H. R. Schlossberg, and H. R. Fetterman, Opt. Commun. 15, 358 (1975).
18. K. N. Rao (unpublished).
19. R. Oberly, K. N. Rao, L. H. Jones, and M. Goldblatt, J. Mol. Spectrosc. 40, 356 (1971).
20. H. R. Gordon and T. K. McCubbin, Jr., J. Mol. Spectrosc. 19, 137 (1966).
21. R. A. McClatchey et al., "AFCRL Atmospheric Absorption Line Parameters Compilation," AFCRL-TR-73-0096, Air Force Cambridge Research Laboratories, Hanscom AFB, MA.
22. J. Finzi and C. B. Moore, J. Chem. Phys. 63, 2285 (1975). These authors have also observed stimulated emission on one 4.3- μ m line by pumping with an optical parametric oscillator.
23. R. V. Ambartsumian, V. S. Letokhov, E. A. Ryabov, and N. V. Chekalin, JETP Lett. 20, 273 (1974).
24. J. L. Lyman, R. J. Jensen, J. Rink, C. P. Robinson, and S. D. Rockwood, Appl. Phys. Lett. 27, 87 (1975).
25. D. M. Larsen and N. Bloembergen, Opt. Commun. (to be published).

III. MATERIALS RESEARCH

A. SURFACE STATES ON TiO_2 AND SrTiO_3

Semiconductor surface states play a key role in the photoelectrolysis of water in cells with TiO_2 and SrTiO_3 anodes. The observation of quantum efficiencies approximating 100 percent in the photogalvanic operation of such cells (when oxygen but no hydrogen is evolved) implies correspondingly high efficiencies for the transfer of photogenerated holes from the semiconductor surface to the oxygen level of the electrolyte. Since this charge transfer takes place by tunneling, which has an appreciable probability only between states of the same energy, both TiO_2 and SrTiO_3 must have electronic states with the same energy as the oxygen level. However, according to our energy level model for photoelectrolysis,^{1,2} neither the conduction nor valence band states of these materials are degenerate in energy with the oxygen level. In each case, the conduction band edge lies close to the hydrogen level of the electrolyte; the valence band edge is located ~ 2 eV below the oxygen level, since the bandgap is ~ 3 eV while the oxygen level is only ~ 1.2 eV below the hydrogen level. Therefore, efficient tunneling requires the existence of surface states lying within the semiconductor bandgap. Evidence for such states located ~ 1.2 eV below the conduction band has been reported by Frank and Bard,³ who investigated the electrochemical behavior of a TiO_2 anode in non-aqueous acetonitrile solutions having a wide range of standard potentials.

In view of the importance of surface states in photoelectrolysis we are using two complementary techniques - electron spectroscopy and photovoltage spectroscopy - to investigate the origin and behavior of these states on TiO_2 and SrTiO_3 . Experiments of the first type are performed with the semiconductor sample in high vacuum, while in the photovoltage experiments the sample is immersed in an electrolyte and functions as an electrode of an electrochemical cell. We report here the results of an electron spectroscopy study of the surface states produced on TiO_2 by Ar-ion bombardment. We also present initial electron spectroscopy data for SrTiO_3 , and initial photovoltage spectroscopy results for both TiO_2 and SrTiO_3 .

1. Two-Dimensional Phases Associated with Defect States on the Surface of TiO_2

We have performed a combined ultraviolet photoemission (UPS), electron energy loss (ELS), low-energy electron diffraction (LEED), and Auger study of defect states on the surface of TiO_2 (rutile) as the defect density is varied by Ar-ion bombardment. From these results, we infer the existence of three different surface defect phases. At low defect densities, Ar-ion bombardment produces extrinsic surface states about 0.7 eV below the TiO_2 conduction band edge that are associated with disorder-induced Ti^{3+} /oxygen-vacancy complexes. As the concentration of defects is increased, a pairing of Ti^{3+} ions similar to that in Ti_2O_3 occurs. Still further bombardment produces ordering of the Ti^{3+} -ion pairs into a Ti_2O_3 -like surface structure. These extrinsic surface states are distinct from the intrinsic gap states to be expected on the surface of TiO_2 due to the truncation of the crystal potential.⁴

All electron spectra were measured with a double-pass cylindrical-mirror spectrometer. Auger and ELS spectra were excited by an electron beam coaxial with the spectrometer, while UPS spectra were excited with the HeI line (21.2 eV) from a microwave discharge lamp. Most of the ELS data were taken with a primary energy of 100 eV at normal incidence.

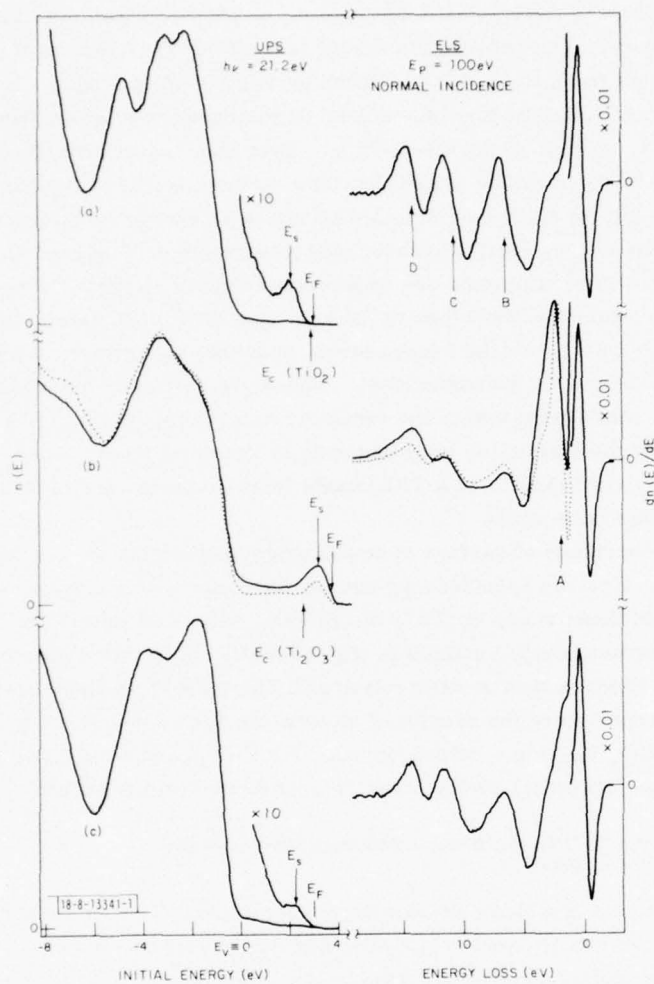


Fig. III-1. Ultraviolet photoemission (UPS) and electron energy loss (ELS) spectra for (a) annealed TiO_2 (110), (b) Ar-ion-bombarded TiO_2 (110) (solid curves) and vacuum-fractured Ti_2O_3 (dotted curves), and (c) Ar-ion-bombarded TiO_2 (110) after exposure to 10^8 Langmuir of oxygen. For UPS, zero of initial state energy is upper edge of valence band.

The surface investigated was a (110) face of a TiO_2 single crystal which was polished and etched, then cleaned by Ar-ion sputter etching and annealed at about 1100 K by electron bombardment in the ultrahigh vacuum system. After annealing, the sample was deep blue, indicating that roughly 10^{19} oxygen vacancies/cm³ had been produced.⁵ The annealed surface exhibited excellent (110) LEED patterns, and no impurities were detected by Auger spectroscopy. To produce surface defects, the sample was then bombarded with 500-eV Ar ions incident at about 20° to the surface plane.

Figure III-1(a) shows the UPS spectrum [photoelectron distribution $n(E)$ vs initial energy E of emitted electrons] and the ELS spectrum [derivative $dn(E)/dE$ of the secondary electron distribution vs energy loss E] for the annealed TiO_2 (110) surface. The UPS spectrum contains a weak peak, with its maximum at an energy E_s about 2.3 eV above the upper edge of the valence band E_v ; this peak is due to excitation of electrons from states lying in the bulk bandgap of TiO_2 , which is 3.05 eV (Ref. 5). These are extrinsic surface states associated with a small density of residual surface defects, since no such peak is observed for vacuum-fractured[†] surfaces of either reduced or unreduced TiO_2 . The Fermi level E_F lies near the bottom edge of the bulk conduction band E_c . The structure in the ELS spectrum of Fig. III-5(a) reflects only three peaks in $n(E)$, labeled B, C and D, that are common to all the surfaces studied here and arise from oxygen-to-Ti cross excitations.⁶

Figure III-1(b) shows the spectra obtained after several minutes of Ar-ion bombardment. In the UPS spectrum the surface-state peak is 50 to 100 times more intense than on the annealed surface, E_s has shifted to 3.2 eV above E_v , E_F has risen to 3.9 eV, and the structure at $E < 0$ associated with the valence band has also changed. The ELS spectrum now exhibits a strong peak (A) at about 1.9 eV that is associated with d-to-d transitions involving Ti^{3+} ions (Ref. 6). Both spectra are remarkably similar to those of vacuum-fractured Ti_2O_3 , which are shown by the dotted curves in Fig. III-1(b). However, the primary-electron-energy dependence of the ELS spectra⁷ shows that ELS peak A is entirely of surface origin in bombarded TiO_2 , but partly of bulk origin in Ti_2O_3 .

When the TiO_2 surface of Fig. III-1(b) was exposed to 10^8 Langmuir of oxygen, the spectra of Fig. III-1(c) were obtained. The intensity of the UPS surface-state peak has been greatly reduced, E_s has shifted back to 2.5 eV, and additional changes have occurred in the valence-band structure. The ELS peak A is much weaker, but has not completely disappeared.

Figure III-2 shows the results of experiments in which an annealed TiO_2 surface was subjected first to a series of Ar-ion bombardments (solid points) and then to a series of oxygen exposures (open points). The abscissa parameter α_s , which is a rough measure of the number of occupied surface states, is the integrated intensity of the UPS surface-state peak (with a linear background subtracted) normalized to its value at the boundary between regions I and II in Fig. III-2 (see below). The value of α_s is lowest for the annealed surface; it is increased by Ar-ion bombardment, and decreased by oxygen exposure. Four quantities are plotted against α_s : (a) $\Delta\Phi$, the difference between the work functions (determined from the UPS spectra) of the treated surface and the annealed surface; (b) $E_F - E_v$; (c) $E_s - E_v$; and (d) the amplitude of ELS peak A, normalized to that of ELS peak C (see Fig. III-1). The last three quantities were very reproducible, and data from two independent runs are plotted in Fig. III-2. The data obtained on initial Ar-ion bombardment fall into three regions as a function of α_s . (The solid lines shown in Fig. III-2 represent least-squares linear fits to the data within either one or two of the

[†]We use the term fractured because TiO_2 and Ti_2O_3 do not cleave well. The surfaces obtained were rough and exhibit poor LEED patterns.

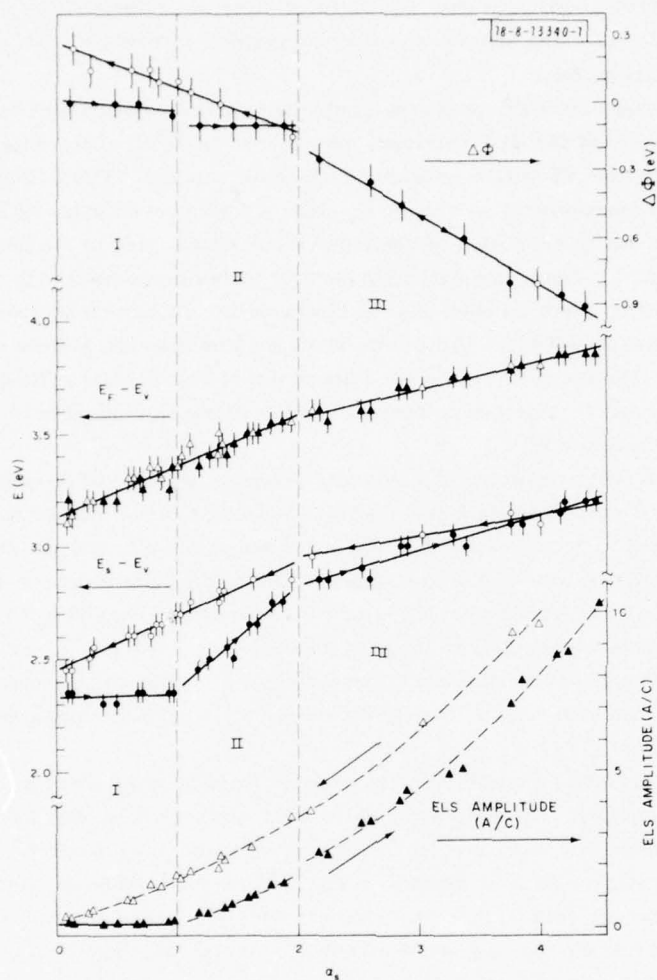


Fig. III-2. Work function change ($\Delta\Phi$), Fermi level ($E_F - E_v$), position of surface-state UPS peak ($E_s - E_v$), and normalized amplitude of ELS peak A vs normalized intensity of UPS surface-state peak (α_s) for Ar-ion bombardment (solid points) and subsequent oxygen exposure (open points) of TiO_2 (110) surface. Arrows indicate sequence in which data were taken.

regions, while the dashed lines are merely smooth curves.) We associate these three regions (designated as I, II, and III) with three different surface phases.

In region I ($\alpha_s < 1$), the intensity of the UPS peak due to the extrinsic surface state increases by more than a factor of 10, but the peak remains 2.3 eV above E_v . The ELS spectra in this region change very little, with no indication of peak A. This shows that the extrinsic state has no well-defined excited state with an energy greater than about 1.2 eV (excited states closer than 1.2 eV to the intense elastic peak could not have been resolved). By $\alpha_s = 1$ the excellent LEED patterns of the annealed surface have virtually disappeared, but the Auger spectra show almost no loss of oxygen. Thus, within region I the atomic arrangement of the surface becomes disordered without appreciable change in surface stoichiometry. Region II ($1 < \alpha_s < 2$) is characterized by the appearance of the sharp ELS peak A, the shifting of the UPS surface-state peak away from the valence band, and a loss of oxygen from the surface. These results indicate that a different type of extrinsic surface state, associated with surface reduction, is being created in region II; it has a ground-state energy higher than that of the state in region I and a well-defined excited state. Region III ($\alpha_s > 2$) is defined by a decrease in the slope of $(E_s - E_v)$ vs α_s by a factor of 3 and by a sharp decrease in $\Delta\Phi$. The position and amplitude of ELS peak A vary smoothly through regions II and III, and only a small change in the slope of $(E_F - E_v)$ vs α_s is seen at $\alpha_s = 2$.

When the heavily reduced, disordered TiO_2 surface ($\alpha_s > 4$) is exposed to oxygen at room temperature, $(E_F - E_v)$ is reversible and E_s remains 0.7 eV below E_F over the entire range of α_s . All four measured quantities vary smoothly for $\alpha_s < 2$. Sufficient exposure to oxygen reduces α_s almost to zero. If the surface is then bombarded with Ar ions, α_s is again increased, and the data essentially reproduce the curves obtained during oxygen exposure.

The constant value of $(E_s - E_v)$ in region I indicates that the surface defects created are noninteracting. However, the data do not permit a determination of the exact nature of these defects. One likely possibility is a vacancy resulting from the displacement of an oxygen ion from a Ti-Ti bridge site to another site, perhaps to a position over one of the fivefold coordinated surface Ti ions. This vacancy has an attractive Madelung potential and is capable of trapping an electron to form a Ti^{3+} /oxygen-vacancy complex. The ground-state energy of this complex would be below the bulk conduction-band edge in TiO_2 , consistent with the observed value of $(E_s - E_v)$.

The discontinuities observed at $\alpha_s = 1$ indicate the occurrence of a surface phase transition, which we interpret as the beginning of strong interaction between surface Ti^{3+} ions. At this point, the sample has been hit by an average of one Ar ion per surface unit cell, as determined from measured ion-beam parameters. The appearance of peak A in the ELS spectrum and the rise of $(E_s - E_v)$ toward its value in Ti_2O_3 are strong evidence for the formation of pairs of Ti^{3+} ions that share a common oxygen octahedral face.⁸ The bonding and antibonding states derived from the 3d orbitals of such Ti^{3+} pairs constitute the conduction bands in Ti_2O_3 (Ref. 8), and we believe that ELS peak A is due to a transition between such pair states. We attribute the onset of pairing at $\alpha_s = 1$ to the Madelung destabilization of the TiO_2 surface structure due to the presence of a high density of surface Ti^{3+} and O^- ions (Ref. 9). The surface is then stabilized by a loss of oxygen and the displacement of some of the Ti^{3+} ions into empty octahedral sites that exist 1.6 Å below the unreconstructed TiO_2 (110) surface, forming Ti_2O_3 -like Ti^{3+} pairs.

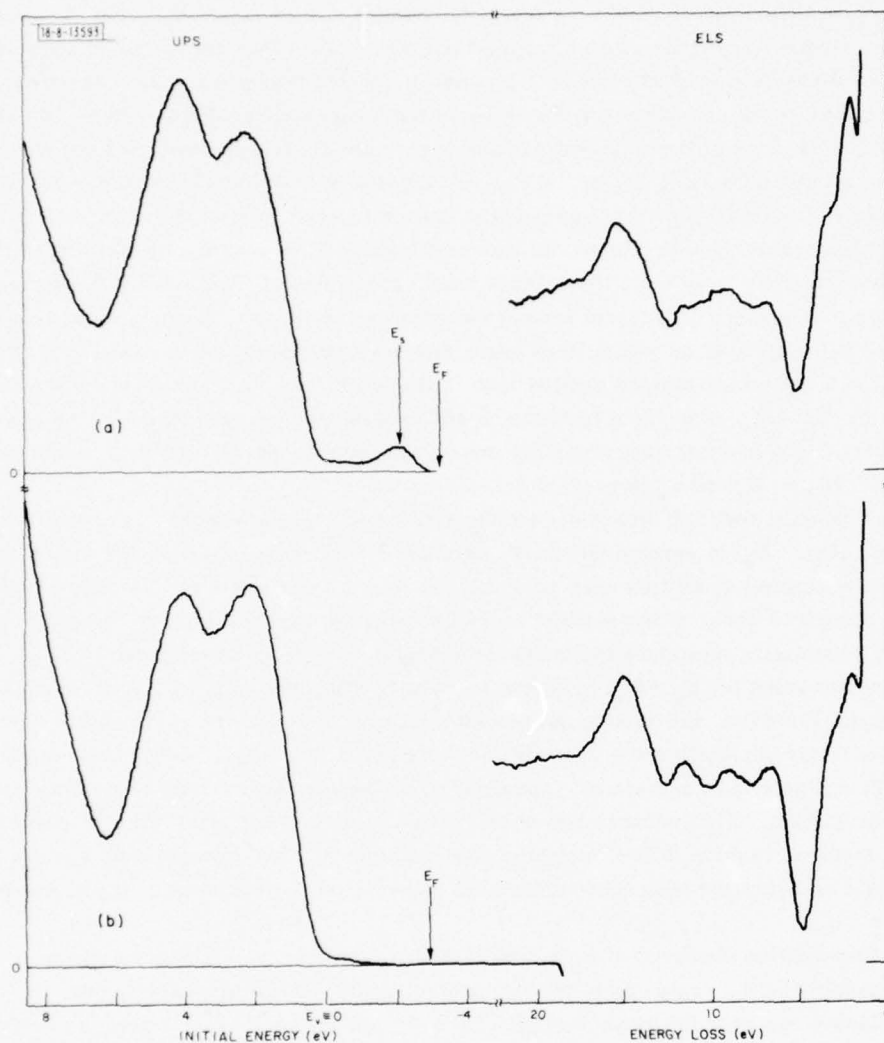


Fig. III-3. UPS and ELS spectra for (a) annealed $\text{SrTiO}_3(100)$ surface and (b) annealed $\text{SrTiO}_3(100)$ surface after exposure to 10^6 Langmuir of O_2 . For UPS, zero of initial state energy is upper edge of valence band.

As the density of Ti^{3+} pairs increases, a cooperative phase transition associated with the ordering of the pairs occurs at $\alpha_s = 2$. In effect, small areas of Ti_2O_3 begin to form on the surface, causing the average work function to decrease toward the lower values that we have observed for vacuum-fractured Ti_2O_3 . The value of $(E_s - E_v)$ continues to rise in region III as more Ti^{3+} pairs are created at the expense of the defects present in region I. After long Ar-ion bombardment times, α_s reaches a constant value of 4 to 5. At this point, the UPS and ELS spectra are almost indistinguishable from those of Ti_2O_3 [see Fig. III-1(b)], confirming the similarity of the two surface structures. Furthermore, vacuum-fractured single-crystal Ti_2O_3 follows oxidation curves similar to those for heavily ion-bombarded TiO_2 , providing additional evidence for this similarity.

2. Electron Spectroscopy of SrTiO_3 Surfaces

Initial studies of SrTiO_3 have been performed on annealed (111) surfaces that yield LEED patterns indicating a high degree of surface order. The UPS and ELS spectra obtained for such a surface are plotted in Fig. III-3(a). The UPS data show that the Fermi level E_F lies 3.15 eV above the valence band edge. Since the room-temperature bandgap of SrTiO_3 is 3.17 eV (Ref. 10), this implies that the sample is n-type, presumably because of bulk reduction that occurred during annealing. (Reduced samples were also used in the photoelectrolysis experiments reported previously.²) A peak due to an electronic state lying within the bulk bandgap of SrTiO_3 is observed in the UPS spectrum at an energy E_s that is 0.9 eV below E_F . The ELS spectrum shows the existence of low-lying excited states at 1.6 and 3.0 eV, as well as peaks at 5.6, 8.2, and 13.5 eV associated with O-Ti cross transitions.⁶

Significant changes in the electron spectra take place when the annealed SrTiO_3 surfaces are exposed to oxygen. The LEED patterns have a slightly higher background intensity, presumably due to the presence of randomly adsorbed oxygen. Figure III-3(b) shows the UPS and ELS spectra obtained for the sample of Fig. III-3(a) after an O_2 exposure of 10^6 Langmuir. The peak at E_s in the UPS spectrum has disappeared, and E_F has dropped to 2.8 eV above E_v , slightly below the bottom edge of the bulk conduction band. Since E_F still lies above E_s , the absence of photoemission at E_s shows that the state responsible for the peak at this energy has been removed by the interaction of the surface with adsorbed oxygen, and therefore that this is a surface state. The ELS peaks at 1.6 and 3.0 eV decrease in intensity with exposure to oxygen, indicating that they are associated with the surface state. The O-Ti cross transitions are also modified by oxygen adsorption, with an additional peak at 10.9 eV appearing in the ELS spectrum.

As pointed out above, the efficient charge transfer between the semiconductor anode and electrolyte that takes place during photoelectrolysis requires the existence of surface states lying within the semiconductor bandgap. The SrTiO_3 surface state revealed by UPS is located at an energy that would permit it to participate in charge transfer. In order to obtain further information concerning the role of this or other surface states in photoelectrolysis, the effect of surface disorder and adsorbed molecules (e.g., H_2O , H_2) on SrTiO_3 surfaces will be studied by electron spectroscopy, and the results will be correlated with those obtained in photoelectrolysis experiments on SrTiO_3 electrodes with similar surfaces.

3. Photovoltage Spectroscopy of TiO_2 and SrTiO_3 Surfaces

To study the electronic states on TiO_2 and SrTiO_3 surfaces while they are immersed in an electrolyte, in situ measurements are being made of the open-circuit AC photovoltage generated

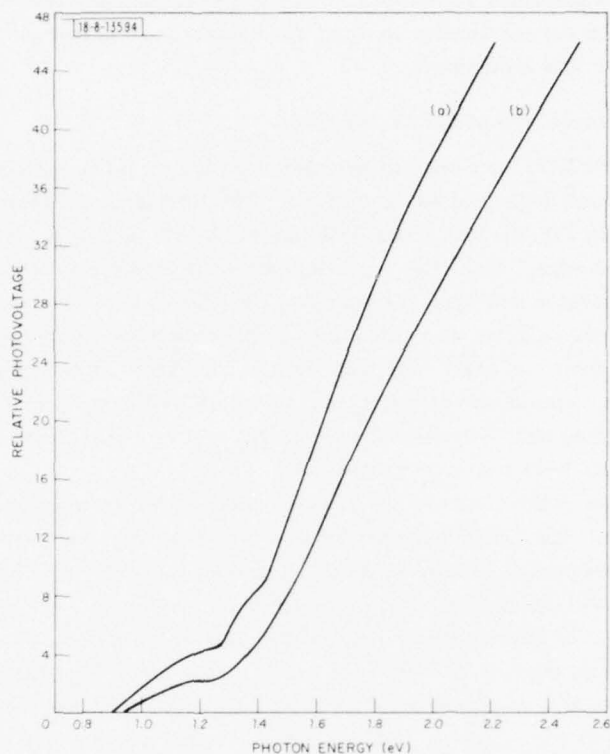


Fig. III-4. Wavelength dependence of relative AC photovoltage generated between polycrystalline TiO_2 anode and Pt cathode when TiO_2 was exposed to chopped radiation with photon energies less than its energy gap. Curves (a) and (b) were obtained with electrodes immersed in 10 M NaOH electrolyte saturated with N_2 and O_2 , respectively.

between the semiconductor anode and platinum cathode of an electrochemical cell when the anode is exposed to chopped radiation with photon energies less than the energy gap. Initial results for a polycrystalline TiO_2 anode are shown in Fig. III-4, where the relative photovoltage generated across a $10^7 \Omega$ load resistor at a chopping frequency of 40 Hz is plotted against photon energy. Similar results are obtained with single-crystal anodes. The photovoltage decreases smoothly with decreasing photon energy, except in the region of 1.2 to 1.4 eV. We attribute the structure observed in this region to transitions involving a surface state, as suggested by the fact that the magnitude of the structure depends on whether the electrolyte is saturated with nitrogen or with oxygen. A surface state located 1.2 to 1.4 eV below the conduction band of TiO_2 could participate in charge transfer between the anode and the oxygen level of the electrolyte.

Similar photovoltage results are obtained with SrTiO_3 anodes, but in this case the effects of chemisorbed oxygen are more pronounced and varied, probably because of the larger band bending at the SrTiO_3 -electrolyte interface.² For photon energies between about 0.9 and 2 eV, exposure of the electrolyte to oxygen produces a large positive photovoltage with some samples, and a large negative photovoltage with others. In preliminary experiments, we have observed a correlation between the sign and magnitude of the photovoltage and the efficiency of photoelectrolysis with the same anode. This behavior will be investigated further by making measurements on samples that have been characterized both by electron spectroscopy and by a variety of analytical techniques.

G. Dresselhaus J. G. Mavroides
V. E. Henrich H. J. Zeiger
D. F. Kolesar

B. SELECTIVE BLACK ABSORBERS USING MgO/Au CERMET FILMS

In solar collectors, an absorber is used to convert solar radiation into thermal energy that is transferred from the absorber to a working fluid such as water or air. The conversion efficiency is limited by thermal losses from the heated absorber due to conduction, convection, and radiation. Since the thermal radiation emitted by objects at terrestrial temperatures is concentrated in the infrared region of the spectrum, radiation losses can be reduced by using selective black absorbers that have low infrared emittance but still have high solar absorption. Although in principle a single material could have both these properties, the selective black surfaces now available are composites prepared by coating a metal having high infrared reflectivity (i.e., low infrared emittance, by Kirchhoff's law) with a thin film that is transparent in the infrared but highly absorbing in the visible, where solar radiation is concentrated.

Several types of thin films with optical properties suitable for preparing selective black surfaces are now available. However, they are not stable at the absorber operating temperatures required for solar/thermal/electric conversion, which may range from 400° to 1000°C. Thus, Ni-black and Cu-black are unstable above 200°C, and Cr-black is not stable much above 300°C. Although the properties of Cr-black are not well understood, our x-ray diffraction data for this material suggest that it is a cermet film consisting of polycrystalline Cr_2O_3 and amorphous Cr metal. If this is the case, the failure of Cr-black at elevated temperatures may result from the crystallization of the Cr or from its oxidation, which occurs at 350°C in air. In an attempt to avoid these problems, we are investigating the preparation of selective black surfaces with a coating of the cermet MgO/Au , which might be expected to exhibit better high-temperature stability because the Au metal is present in crystalline form and does not oxidize in air.

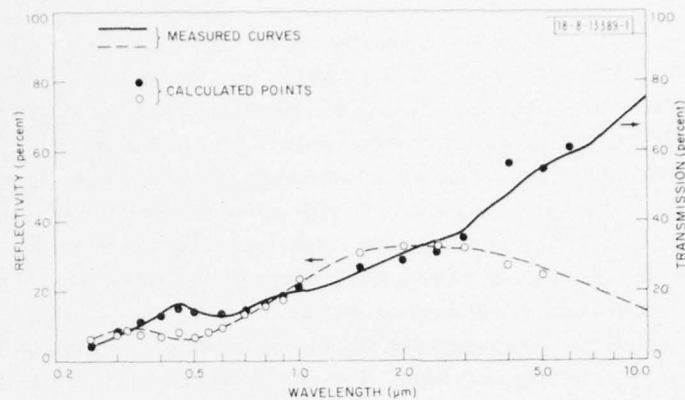


Fig. III-5. Transmission (solid curve) and reflectivity (dashed curve) measured for 1500-Å-thick MgO/Au film on BaF₂, compared with calculated points representing best fit obtained for model using three Lorentzian oscillators to represent optical properties of film.

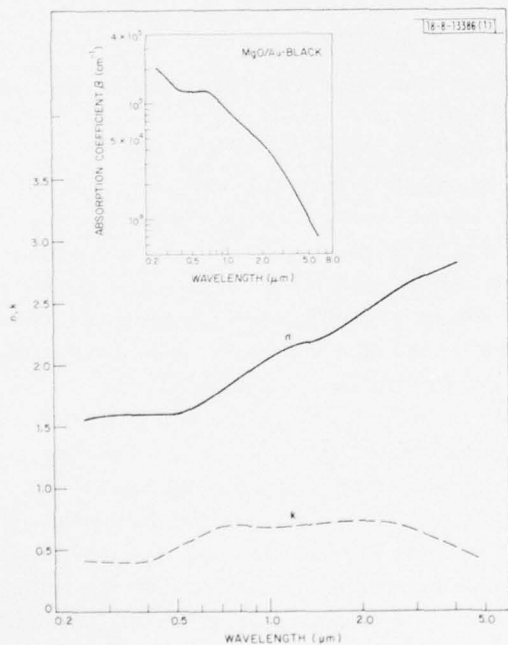


Fig. III-6. Wavelength dependence of refractive index n and extinction coefficient k calculated for MgO/Au film from transmission and reflectivity data of Fig. III-5.

Fine-grained MgO/Au films were prepared by RF sputtering from a hot-pressed 12.7-cm-diameter composite target containing 75 vol% MgO and 25 vol% Au. (A detailed description of the preparation technique has been reported previously.¹¹) Sputtering was performed at 13.56 MHz in Ti-purified Ar gas at 7×10^{-3} Torr (N_2 equivalent). The films were deposited at a rate of about 50 Å/min. on various metal substrates that were placed on a water-cooled stainless-steel platform. Some films were deposited on single-crystal BaF_2 substrates in order to permit evaluation of their optical properties. Transmission electron microscope studies showed that the films consist of discrete MgO and Au crystallites ranging in size from about 10 to 200 Å.

Figure III-5 shows the wavelength dependence of the optical transmission (solid line) and reflectivity (dashed line) measured for a 1500-Å-thick MgO/Au film on BaF_2 . The data have been fitted to a good approximation by representing the complex dielectric constant of the film in terms of the sum of three Lorentzian oscillators, and by using a multilayer matrix formulation to take account of the fact that the observed properties are those of a film- BaF_2 composite. A nonlinear minimization routine was utilized to determine the adjustable parameters of the three oscillators that would yield the best fit to the data. The results of the calculation are represented by the open (reflectivity) and closed (transmission) points plotted in Fig. III-5.

Figure III-6 shows the wavelength dependence of the refractive index n and extinction coefficient k calculated for the MgO/Au film from the transmission and reflectivity data of Fig. III-5. The absorption coefficient $\beta = 4\pi k/\lambda$, where λ is the wavelength, is plotted in the inset. The values of β are such that a film 1500 Å thick will absorb almost all the solar radiation, but will transmit almost all the infrared radiation at wavelengths longer than 4 μ m. Therefore, good selective black absorbers should be obtained by depositing MgO/Au films on metals with high infrared reflectivity. This expectation has been confirmed by measuring the spectral reflectivity $R(\lambda)$ for surfaces obtained by depositing 1500-Å-thick MgO/Au films on copper, aluminum, 304 stainless steel, and 304 stainless steel coated with a molybdenum film 1000 Å thick. The solar absorptivity α and infrared emissivity ϵ are defined respectively as

$$\alpha = \frac{\int_{0.25 \mu m}^{2.5 \mu m} [1 - R(\lambda)] A_m(\lambda) d\lambda}{\int_{0.25 \mu m}^{2.5 \mu m} A_m(\lambda) d\lambda}$$

and

$$\epsilon = \frac{\int_{1 \mu m}^{100 \mu m} [1 - R(\lambda)] W_B(T_B, \lambda) d\lambda}{\int_{1 \mu m}^{100 \mu m} W_B(T_B, \lambda) d\lambda}$$

where $A_m(\lambda)$ is the solar radiation spectrum at air mass 2, and $W_B(\lambda)$ is the blackbody radiation function for a temperature T_B of 121°C. In every case, α was between 0.90 and 0.93. The value of ϵ was determined by the infrared reflectivity of the substrate, and ranged from 0.04 for copper to 0.1 for stainless steel.

To investigate the stability of the MgO/Au-metal composites, spectral-reflectivity measurements were repeated after the samples had been heated in ambient air for several days at various temperatures. The film-copper samples are stable only to about 200°C, while the optical properties of those prepared with stainless steel and aluminum begin to degrade above about 300°C. In these cases, α decreases but ϵ does not change substantially. The optical properties obtained by depositing MgO/Au films on stainless steel coated with 1000-Å-thick

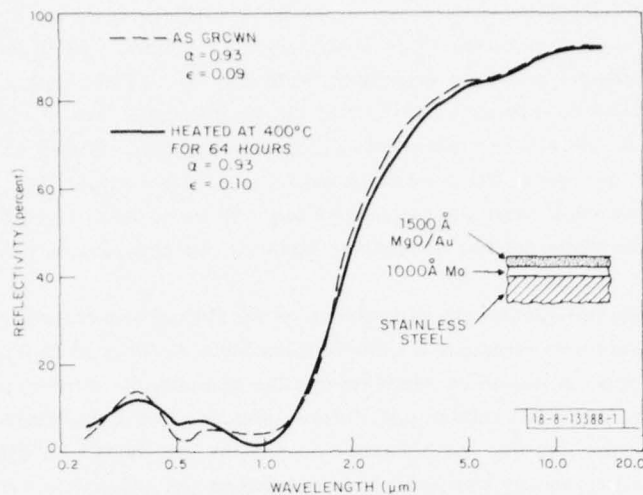


Fig. III-7. Reflectivity measured before and after heating for sample prepared by depositing MgO/Au film on molybdenum-coated stainless steel.

molybdenum are stable up to 400°C, as shown by Fig. III-7, which compares the reflectivities measured for a sample that was not heat treated and for a sample that had been heated in air to 400°C for 64 hr. Although the spectra differ slightly, α is 0.93 for both samples and ϵ is essentially the same. Degradation began to occur when similar samples were heated to 500°C, which caused α to decrease without changing ϵ . Examination of the samples with a scanning electron microscope revealed crack formation and subsequent surface aggregation, which did not occur for samples heated to only 400°C. These observations suggest that the degradation at 500°C resulted from differences in the thermal expansion coefficients of the materials.

J. C. C. Fan
P. M. Zavracky

REFERENCES

1. J. G. Mavroides, D. I. Tchernev, J. A. Kafalas, and D. F. Kolesar, Mater. Res. Bull. 10, 1023 (1975), DDC AD-A017419/3.
2. J. G. Mavroides, J. A. Kafalas, and D. F. Kolesar, Appl. Phys. Lett. 28, 241 (1976), DDC AD-A025630.
3. S. N. Frank and A. J. Bard, J. Am. Chem. Soc. 97, 7424 (1975).
4. F. J. Morin and T. Wolfram, Phys. Rev. Lett. 30, 1214 (1973); T. Wolfram in Electrocatalysis on Non-Metallic Surfaces (N. B. S. Special Publication, to be published).
5. D. C. Cronmeyer, Phys. Rev. 87, 876 (1952).
6. V. E. Henrich, H. J. Zeiger, and G. Dresselhaus, in Electrocatalysis on Non-Metallic Surfaces (N. B. S. Special Publication, to be published); Solid State Research Report, Lincoln Laboratory, M. I. T. (1975:1), pp. 38-42, DDC AD-A009848/3.
7. V. E. Henrich, G. Dresselhaus, and H. J. Zeiger, Phys. Rev. Lett. 36, 158 (1976).
8. J. B. Goodenough, Prog. Solid-State Chem. 5, 145 (1972).
9. G. Dresselhaus, H. J. Zeiger, and V. E. Henrich, Bull. Am. Phys. Soc. 21, 321 (1976).
10. K. W. Blazey, Phys. Rev. Lett. 27, 146 (1971).
11. J. C. C. Fan and V. E. Henrich, J. Appl. Phys. 45, 3742 (1974), DDC AD-A002774/8.

IV. MICROELECTRONICS

A. CHARGE-COUPLED DEVICES

In a previous report,¹ we noted that a phosphorous gettering step at the end of the fabrication process appeared to be of benefit in lowering the dark current in the CCD imaging arrays being developed for the GEODSS (Ground Electro-Optical Deep Space Surveillance) Program. At that time, dark currents as low as 5 nA/cm^2 had been measured on gate-controlled diodes which are included on the chip next to the 30×30 CCD imaging array. Dynamic tests on the CCD itself were begun to verify the dark currents predicted by the gated-diode measurements. Unfortunately, the device yield on the gettered wafer was quite low, and only a very limited amount of data could be obtained.

The dark current was measured on these devices by the usual method of holding the clock lines at a fixed DC level for a period of time in order to collect the thermally generated charge in the CCD. The normal clocking sequence is then started, and the collected charge is transferred out of the device. On the tested devices, only the 32-bit output register was functioning, and the data discussed here were obtained on that part of the device.

The room-temperature dark current on the best devices was relatively uniform from well-to-well, with the exception of a few wells having dark currents in excess of 150 nA/cm^2 . A comparison was made between the low, uniform dark currents in the CCD and the dark currents from the gated diodes biased to the same potentials. Of two devices so tested, dark currents of 27 and 36 nA/cm^2 were measured on the CCD, compared with 18 and 35 nA/cm^2 , respectively, from the gated diodes. This correlation gives added confidence to the gated diode measurements as indicators of the average CCD dark current. However, since the gated diodes cover an area equal to about 60 CCD wells, localized dark-current spikes cannot be detected in such measurements.

B. E. Burke
W. H. McGonagle

B. ALIGNMENT OF THE 100×400 -ELEMENT ARRAYS FOR THE GEODSS CCD SENSOR

The design of the sensor for use at the prime focus of the 31-in. telescope being used in the GEODSS Program was described in an earlier report (see p. 46 in Ref. 1). It is a hybrid integrated circuit utilizing 16 charge-coupled-device, 100×400 -element imaging arrays mounted on an alumina substrate. Each array is contained on a 0.135×0.516 -in. chip. This hybrid sensor is shown in Fig. IV-1. The alignment requirements for this sensor are such that a column of sensing elements on any one chip must align with the appropriate column on all chips above and below it within 0.0004 in. (0.4 mil). It is further required that the center lines of all chips must not vary more than 0.03° from parallelism.

The chip alignment tolerances are impossible to achieve with normal mounting techniques, so a specialized mounting procedure had to be developed. A measuring coordinator (designed for the inspection of machined parts) capable of being positioned to better than 0.2 mil in x and y has been modified so that its inherent accuracy can be utilized in the chip placement process. A borosilicate glass vacuum chuck has been designed and fitted to the coordinator stylus. Each chip is picked up at a locating and aligning station adjacent to the substrate, and is then precisely located over a predetermined position on the substrate which has been coated with an

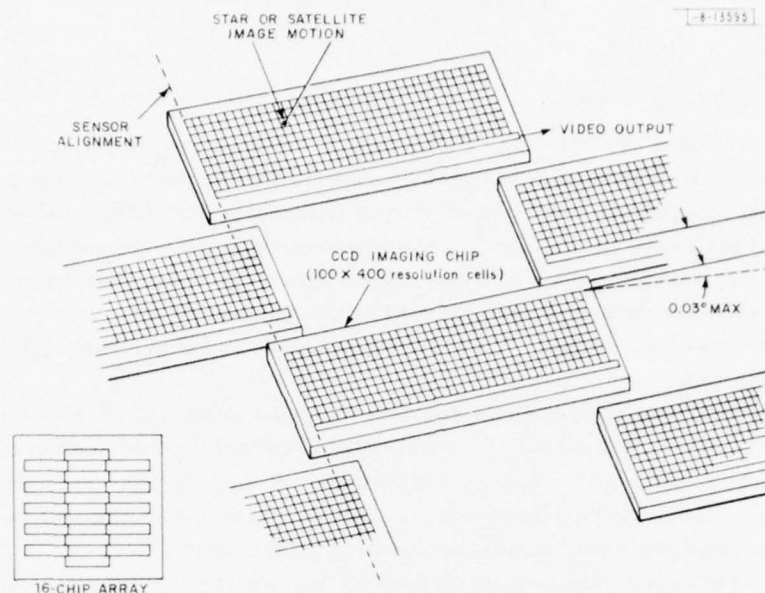


Fig.IV-1. Section of 16-chip hybrid sensor showing several of 100- \times 400-element CCD imaging arrays. Each column on an individual device must be aligned within 0.0004 in. of corresponding columns on all devices above and below it. Grids on each device must be parallel with grids on all other devices within 0.03°.

anerobic, quick-setting adhesive. The chip is lowered to the substrate and held in position for 3 min., allowing the adhesive to set. The vacuum is then released and the chuck lifted off the chip with a micrometer-type screw. This procedure allows the accurate placement of each chip at a known coordinate location on the substrate, which insures that the tolerance requirements are met and the chip is replaceable, if necessary.

The above procedure requires that the CCD chips be precisely sawed from the wafer, accurate and square to within 0.1 mil. Several problems have developed in our efforts to attain this precision which approaches the state of the art. Blade vibration caused by the shaft bearing makes it very difficult to accurately define and position the magnified edge of the saw during rotation. Further, the thermal expansion of the shaft supporting the saw blade results in a loss of parallelism in test pieces. Renovation of the saw including the installation of an improved shaft bearing is under way, and is expected to permit chips to be cut to the specification of ± 0.1 mil.

Dimensional characterization of both the individual chip and the 16-chip layout has been facilitated by the fitting of a high-precision, specially selected x-y stage to our profile projector. Procedures have been developed which enable us to obtain reproducible digital read-outs (under 200X magnification) to within 50 microinches. By selecting the mechanical test chips most nearly meeting dimensional specifications and utilizing the procedures described above, we have aligned and attached 16 chips on a 2 \times 2 alumina substrate within the specified 0.4-mil tolerance in both the x and y axes. This accuracy is based on edge measurements.

T. F. Clough
L. L. Grant

C. HIGH-EFFICIENCY ION IMPLANTED GaAs IMPATT DIODES

A DC-to-RF conversion efficiency of 37 percent combined with an output power of 3.4 W has been obtained at 3.3 GHz from a Schottky-barrier GaAs IMPATT diode having an implanted lo-hi-lo profile. The donor spike was produced by implanting silicon into an epitaxial layer with an n-type concentration of $1.65 \times 10^{15} \text{ cm}^{-3}$. This implantation technique has resulted in a very high yield of lo-hi-lo profile devices with efficiencies greater than 30 percent.

The material and device fabrication procedures for these diodes have been described previously,² and the recent results of RF measurements on these devices are presented in this report. Measurements were made in a coaxial circuit using two quarter-wavelength transformers for tuning. The heat sink for the devices, a $\frac{1}{2}$ -in.-diameter copper stud, was air cooled. The best results, measured on an individual device from four of the five wafers processed, are given in Table IV-1. The first two devices in the table are from wafers taken from different regions of an epitaxial slice which had a background carrier concentration of $1.75 \times 10^{15} \text{ cm}^{-3}$. The two wafers were given implant doses of 3.2 and $3.6 \times 10^{12} \text{ cm}^{-2}$, respectively. The Si^+ ion energy was 250 keV for both implants. As was expected, the lower dose results in a larger depletion width, higher breakdown voltage, and a lower optimum frequency. For this epitaxial layer carrier concentration, the lower dose yielded the higher efficiency. The third and fourth devices in Table IV-1 are on wafers from an epitaxial slice with a background concentration of $1.65 \times 10^{15} \text{ cm}^{-3}$. The two wafers were implanted with doses of 3.2 and $3.5 \times 10^{12} \text{ cm}^{-2}$, respectively. With the slightly lower background density of this epitaxial slice, both dose levels result in devices with a larger depletion width, higher breakdown voltage, and lower optimum frequency than the values measured for the previous wafers. On wafers from the $1.65 \times 10^{15} \text{ cm}^{-3}$ slice, the higher dose yielded the higher efficiency. The maximum efficiency of 37 percent shown in Table IV-1 was obtained at a current of 65 mA and an operating voltage of 140 V.

TABLE IV-1
RF TEST RESULTS OBTAINED FROM ION IMPLANTED LO-HI-LO GaAs IMPATT DIODES[†]

Epitaxial Layer Carrier Density ($\times 10^{15} \text{ cm}^{-3}$)	Implant Dose [‡] ($\times 10^{12} \text{ cm}^{-2}$)	Reverse Voltage at 1 mA (V)	RF Output Power (W)	Frequency (GHz)	DC-to-RF Efficiency (percent)
1.75	3.2	101	3.0	3.7	32
1.75	3.6	55	1.7	4.7	26
1.65	3.2	130	2.6	2.8	28
1.65	3.5	104	3.5	3.3	37

[†] These are the best results from four different wafers. The devices were tested in a coaxial circuit and were air cooled.

[‡] All implantations were made using 250-keV Si^+ ions.

In Table IV-2 the spread of the RF results for two of the wafers, one from each epitaxial layer concentration, is given. The group of five diodes is from a wafer which includes the second device of Table IV-1, and all had similar performance. Four out of the five devices had efficiencies in the range 20 to 26 percent. The group of 19 devices in Table IV-2 is on the wafer which includes the fourth device of Table IV-1. These 19 devices were picked at random from the 70 diodes having a hard breakdown (reverse leakage $<10 \mu\text{A}$ at 1 V below breakdown) on that wafer. All but one of these devices performed at better than 30 percent efficiency, and three performed at better than 35-percent efficiency.

TABLE IV-2 UNIFORMITY OF DC-TO-RF EFFICIENCY FOR TWO GROUPS OF DEVICES FABRICATED FROM TWO DIFFERENT IMPLANTED WAFERS							
Number of Diodes Tested	Reverse Voltage at 1 mA (V)	Output Power (W)	Frequency (GHz)	Number of Diodes with Efficiency Greater Than (percent)			
				20	25	30	35
5	49 to 55	1.0 to 1.7	4.7 to 5.0	4	2	0	0
19	85 to 104	2.8 to 3.5	3.2 to 3.6	19	19	18	3

It is a result of the control provided by the implantation technique that 37-percent efficiency has been achieved for a diode on only the fifth wafer to be processed. In addition, improvements of the already quite high device yields should be possible. Better control of nitride thickness and uniformity, or implantation into a bare surface followed by encapsulation should yield better device uniformity. Moreover, the implant energy has not been optimized. Even without further improvements, however, these results indicate that silicon implantation can be used to produce lo-hi-lo IMPATTs with higher device yields and efficiencies than have been achieved with epitaxial techniques.

C. O. Bozler R. W. Laton (Group 33)
J. P. Donnelly R. W. Sudbury (Group 33)
R. A. Murphy W. T. Lindley

D. DOUBLE-RETICLE TECHNIQUE FOR ELIMINATING PHOTOREPEATED DEFECTS IN PHOTOMASKS FOR LSI

As the die size for LSI circuits grows larger and the circuits more complex, fabricating masks free of photorepeated defects becomes more difficult. These defects are often the result of dirt or emulsion defects in the clear areas of the 10X reticle. Since we are using chrome photoresist sensitized with positive photoresist, defects as small as $6 \mu\text{m}$ on the reticle can be resolved at 0.1X, and therefore cannot be tolerated. Furthermore, a die size of $1/4$ in. implies a 6-in.^2 area on the reticle which must be free of dirt and defects. The dirt can be removed by a tedious inspection and cleaning procedure, but the gel slugs inherent in the silver halide emulsion used for the 10X reticle are not removable. Further, they seem to be more opaque at the ultraviolet wavelengths used for photoresist exposure than under the visible light used for inspection, a phenomenon which further complicates the inspection problem. Our experience

indicates that high-resolution emulsion photoplates typically have a minimum of two to four defects per square inch, which makes it almost impossible to find one with no defects in a 6-in.² area.

In order to minimize the effect of these defects and to significantly reduce the amount of inspection and cleaning necessary, we have devised a technique of re-exposing the clear areas with a second reticle with slightly oversized geometries. This method is analogous to the double-masking technique sometimes used to combat similar problems when performing photoresist operations at the wafer level. This second exposure removes any images caused by dirt or gel slugs on the first reticle, except immediately adjacent to the patterns. Any defects on the second reticle will not reproduce because the underlying photoresist has already been exposed. It is possible for defects on the two reticles to coincide, but this is highly unlikely.

However, when we are dealing with projected images near the diffraction limit of the lens, some unique problems arise. In order to avoid overexposing the photoresist, the exposure time for each reticle must be reduced somewhat, and the oversized reticle must be exposed after the normal reticle has been exposed. The exposure time is less because some light from the oversized reticle finds its way into the nominal-sized patterns from diffraction and scattering in the optical system, from scattering in the photoresist itself, and from scattering and reflection from the chrome. Also, the optical response of the positive photoresist used is nonlinear — that is, the initial exposure has a greater effect upon the resist than do later equal exposures — and the stray light mentioned above has a greater effect if the oversized reticle is used first.

Using Nikon Ultra-Micro-Nikkor 1/10X and 1/5X g/h-line lenses, we have made the patterns on the oversized reticle (10X or 5X) 0.002 in. larger (0.001 in. in each direction) than the normal-sized patterns. With a projected image size of 0.00015 in. (3.8 μ m), we have found it necessary to reduce exposure time for each reticle by 30 to 40 percent from our normal setting. With black chrome or iron oxide photoresist sensitized plates, or with larger patterns, the reduction in exposure time ranges from 0 to 30 percent.

This technique has been used for the fabrication of masks for the Lincoln ECL Gate Array. This device uses a 0.237- \times 0.238-in. die, and contains 1864 bipolar transistors and their associated diffused resistors. The minimum linewidth for the device is 0.00015 in. The reticles for certain layers were almost 100-percent clear field, and the typical reticle for these layers contained 20 to 30 emulsion defects. This defect level, combined with a long pattern generator running time, had made it virtually impossible to get a useable reticle (i.e., one with all defects in benign locations). With the new double-reticle technique, almost any two reticles from the pattern generator (one with nominal geometries and one with oversized geometries) could be used to make a useable mask with, at most, one or two photorepeated defects.

This double-reticle technique is rapidly becoming a standard procedure for any of our work which requires a positive clear field reticle, and even for some negative masks with unusually large clear areas. We have almost eliminated the problems associated with gel slugs, and reticle cleaning is much less tedious. This technique tolerates a reasonable number of defects and particulates, and only the edges of the geometries on the normal-sized reticle need be defect and contamination free.

D. L. Smythe
T. Herndon (Group 23)

REFERENCES

1. Solid State Research Report, Lincoln Laboratory, M.I.T. (1975:4), p. 45, DDC AD-A025489.
2. Ibid. (1976:1), p. 62.

V. SURFACE-WAVE TECHNOLOGY

A. CONTINUOUSLY VARIABLE-DELAY-LINE SYSTEM

A continuously variable-delay-line system using surface-acoustic-wave dispersive delay lines in the reflective-array-compressor (RAC) configuration¹ has been designed and developed for the satellite communications program. The system is intended for adaptive cancellation of multipath signals arriving up to 30 μ sec after the direct signal. A configuration particularly well suited for this application uses a pair of dispersive delay lines operating in cascade, two mixers, and a voltage-controlled oscillator (VCO). Delay variations are obtained by suitably changing the VCO control voltage. Considerations of bandwidth and dispersion for such a system show that devices with relatively large time-bandwidth products are needed for implementing variable delay lines in this manner. Variable delay lines employing dispersive devices have been previously studied,²⁻⁴ but have not found widespread use because of the lack of high-quality large-time-bandwidth dispersive delay lines. The RAC configuration is particularly well suited for meeting this requirement and, in fact, RAC devices make it possible to implement this adaptive system.

The circuit configuration for the continuously variable delay line is illustrated in Fig. V-1(a). The linear dispersion curves representative of each RAC device are indicated in Fig. V-1(b).

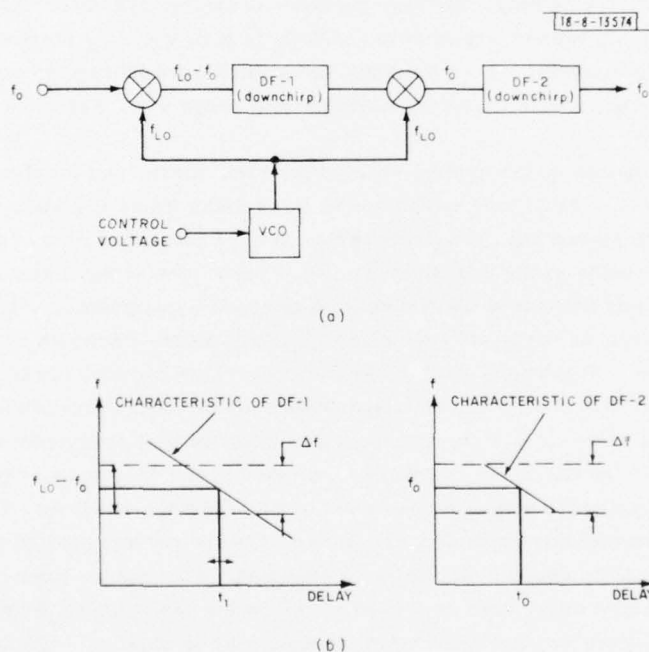


Fig. V-1. (a) Variable-time-delay system using surface-acoustic-wave dispersive delay lines. (b) Linear dispersion curves characteristic of each dispersive filter. Delay (t_1) through DF-1 is controlled by output frequency (f_{LO}) of VCO. Input signal bandwidth is represented by Δf .

Both units have identical dispersion slopes with nonoverlapping frequency bands. The incoming signal (70 ± 5 MHz) is mixed with the output of the VCO (165 ± 5 MHz) which controls the delay through the first dispersive filter (DF-1). The output from this first device (95 ± 10 MHz) is spectrally inverted in a second mixer (the difference frequency is selected) wherein the VCO frequency is removed. The residual dispersion is removed in the second RAC filter (DF-2), which has a 10-MHz bandwidth centered at 70 MHz. The overall delay is nondispersive and a function only of the VCO frequency, provided each delay line has a linear-FM slope.

Full advantage is taken of the excellent filtering characteristics of the RAC devices by separation of the frequency bands of the individual devices and the VCO. Spurious signal levels are thereby reduced to a minimum. At the maximum input signal level which yields an output 75 dB above noise, mixer-related spurious signals are down by a minimum of 70 dB.

One of the design goals for the system is to minimize the time-bandwidth product of the dispersive delay lines. This criterion results in a minimum time-bandwidth product, $\Delta T \Delta f = 1200$ for DF-1. The second RAC unit, DF-2, shown in Fig. V-1 has less stringent requirements on bandwidth and dispersion. The minimum bandwidth requirement on this unit is 10 MHz, with dispersion dependent on the choice of chirp slopes. For the minimum $\Delta T \Delta f$ design of DF-1, the dispersive delay of DF-2 is 30 μ sec, resulting in a device with time-bandwidth product of 300. These device parameters are considered modest based on the group's ongoing and past development programs involving RAC-type structures.

Because the variable-delay system operates in essentially a CW mode, there is a greater need for low insertion loss and larger CW dynamic range than in radar pulse-compression systems wherein correlation gain helps increase the overall system dynamic range. Thus, in order to reduce device insertion loss to a minimum, LiNbO_3 (a high-coupling piezoelectric) was selected as the substrate material. Low-insertion-loss units were fabricated and incorporated in the variable delay line to provide a system with dynamic range in excess of 70 dB for input powers less than 1 mW.

The frequency response of the system at the minimum, mean, and maximum delay intervals is illustrated in Fig. V-2. Amplitude variations at fixed delay times are about 1 dB across the design bandwidth, with approximately 1.5-dB variation over the entire delay range. These variations are largely traceable to the slightly nonuniform responses of the dispersive delay lines. The response of the lines became more nonuniform after we experimented with a new phase-compensation procedure. It is not entirely clear why this modified scheme caused changes in the frequency response. Subsequent dispersive devices, which are already in the process of being phase compensated, will use our standard phase-compensation procedure and thus should provide a system with more uniform response as a function of both frequency and delay.

Fresnel amplitude and phase ripples were minimized in the frequency response of each RAC unit by amplitude weighting the impulse responses of the individual devices. The type of amplitude weighting incorporated consisted of a response flat in the central portion of the impulse response, with approximately cosinusoidal tails on each end. A computer analysis of the frequency response of the dispersive delay lines was used to determine the optimum length of the cosinusoidal tails. The results show that near-optimum weighting is obtained when the cosinusoidal tails of the impulse response have a length equal to $(\Delta T / \Delta f)^{1/2}$, where $\Delta T / \Delta f$ is the nominal linear-FM slope of the impulse response.

Measurements of system phase response at the selected delay times illustrated in Fig. V-2 show approximately 2° rms deviations from linear response. The residual dispersion of the

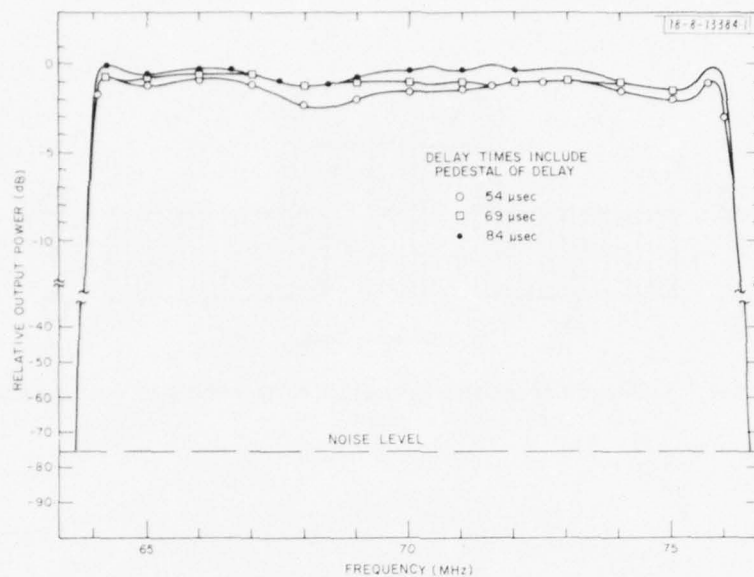


Fig. V-2. Variable-delay-line frequency response at minimum, mean, and maximum delay intervals.

system was calculated from a least-squares linear fit to the phase-response data. The absence of a significant quadratic component in the system response indicates that the chirp slopes of the individual dispersive units are well matched.

The performance of the system was evaluated by delaying various types of signals including short (<50 nsec) wide-band impulses, narrow-band tone bursts, and PSK sequences with 10-MHz chip rates. In all cases, the output appeared as if the input signals had been passed through a square-response filter with a bandwidth slightly in excess of 10 MHz, a response consistent with Fig. V-2.

V. S. Dolat

B. MULTISTRIP COUPLING TO SURFACE-ACOUSTIC-WAVE (SAW) RESONATORS

The multistrip coupler⁵ (MSC) is a very useful SAW component which, among other things, can be used to couple out a certain fraction of the energy in a traveling-wave beam. With the advent of the SAW resonator,⁶ it is natural to consider the use of the MSC as a means of coupling to the resonator. This possibility was first demonstrated experimentally in a rejection-filter application,⁷ and since then has also been theoretically considered in a coupled-resonator filter configuration.⁸ The present work focuses on an understanding of the basic physics of the MSC in a resonant (standing-wave) environment, as opposed to the nonresonant (traveling-wave) regime in which it has been primarily employed to date.

To this end, we have considered the very simple configuration of Fig. V-3. An MSC consisting of a periodic array of 15 Al strips is positioned at an arbitrary location between two grating reflectors which are separated by $10.5 \lambda_0$ edge-to-edge. Together, the gratings form a SAW resonator, resonating at approximately 68.4 MHz. The lower "track" of the MSC aperture lies in the cavity, and the upper "track" lies outside. The Al strips of the MSC are $0.25 \lambda_0$ wide on $0.375 \lambda_0$ centers, whereas the (200) elements in the reflection gratings consist of $0.018 \lambda_0$

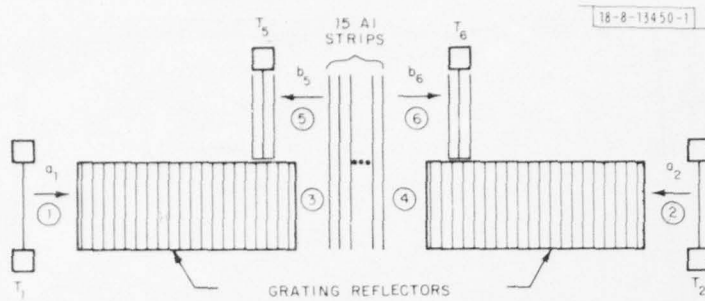


Fig. V-3. Schematic of multistrip-coupled SAW-resonator configuration.

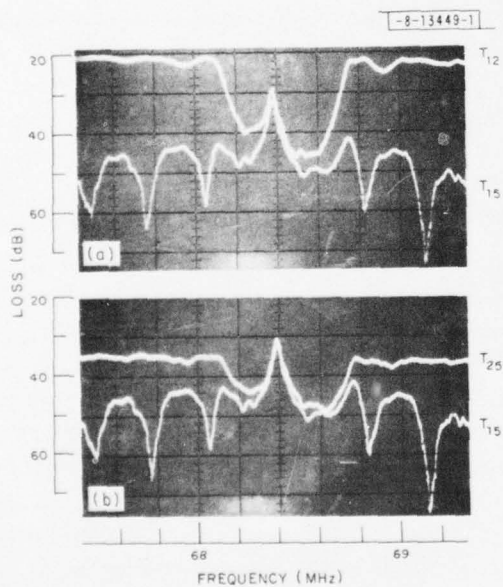


Fig. V-4. (a) Comparison of transmission through resonator T12 with reverse-coupled response T15. (b) Comparison of forward-coupled response T25 with reverse-coupled response T15.

deep grooves, ion-beam etched into the surface of a Y-Z LiNbO₃ substrate. The gratings and surface-wave beams are 100 λ_0 wide. $\lambda_0 = 50.8 \mu\text{m}$ is the wavelength corresponding to the nominal center frequency of the grating stop band. The cavity is excited through the ends by either of transducers T₁ or T₂, and output transducers T₅ and T₆ are situated on each side of the MSC in the upper track.

In the absence of the resonator, the behavior of the intrinsic MSC is such that transducers T₁ and T₅, as well as T₂ and T₆, are decoupled. In the presence of the resonator, however, the backward-traveling component of the standing wave within the cavity leads to a (reverse) coupling between T₁ and T₅, and between T₂ and T₆, in addition to the usual (forward) coupling between T₁ and T₆, and between T₂ and T₅. In view of the fact that the above reverse coupling is associated with a cavity resonance, this effect should be extremely narrow band for a high-Q resonance.

Figure V-4(a) shows a measurement of the transmission T₁₂ through the resonator from transducers T₁ and T₂. The "W" region of T₁₂ corresponds to the stop band of the reflection gratings, and the central peak of the "W" occurs at the cavity resonance. Also shown in Fig. V-4(a) is the reverse-coupled response T₁₅ between T₁ and T₅, which peaks up at resonance, as expected. In addition to this main peak due to the high-Q resonance of the cavity, there are secondary maxima due to low-Q resonances associated with the sidelobes of the reflection coefficient of a finite-length grating.⁹ This sidelobe structure decreases monotonically, and eventually falls off to a level below -75 dB.

The behavior of the device and, in particular, the measured frequency response on resonance in Fig. V-4, can be described in terms of two independent parameters. The first is R, the magnitude of the grating reflection coefficient; the second is c, the magnitude of the scattering coefficients S₃₆ = S₄₅ of the intrinsic 4-port MSC (Ref. 10) shown in Fig. V-3. For the 200-groove gratings used in this device, calculations¹¹ show that in the center of the stop band R = 0.96. The value of c for the MSC can be accurately measured in a simple manner from the response T₂₅ shown in Fig. V-4(b). For the above configuration of 15 strips, it is found that c = 0.27.

An analysis of the problem shows that when the frequency and the separation of the gratings satisfy the phase condition for resonance,⁹ the acoustic coupling (not including transducer losses) between ports 1 and 5 (or 2 and 6), and between ports 2 and 5 (or 1 and 6) is given by the expressions:

$$\left| \frac{b_5}{a_1} \right| = cT \left[\frac{Rt}{1 - R^2 t^2} \right] \quad (\text{V-1})$$

and

$$\left| \frac{b_5}{a_2} \right| = cT \left[\frac{1}{1 - R^2 t^2} \right] \quad (\text{V-2})$$

where a_1 , a_2 , and b_5 are wave amplitudes defined in Fig. V-3. In addition, $T = (1 - R^2)^{1/2}$ is the transmission-coefficient magnitude for the individual grating reflectors, and $t = (1 - c^2)^{1/2}$ ($= |S_{34}| = |S_{56}|$) is the magnitude of the "straight-through" transmission coefficient for the intrinsic MSC. Using Eqs. (V-1) and (V-2) along with the measured transducer conversion efficiencies, the experimental results of Fig. V-4 can be predicted to within a decibel.

R. C. M. Li
J. A. Alusow

REFERENCES

1. R. C. Williamson and H. I. Smith, IEEE Trans. Microwave Theory Tech. MTT-21, 195 (1973), DDC AD-772211/9.
2. J. Burnsweig, W. T. Gasser, and S. H. Arneson, "Electrically Controllable Time Delay," IEEE 1973 International Microwave Symposium Digest, pp. 134-136.
3. E. G. S. Paige, "Dispersive Filters: Their Design and Application to Pulse Compression and Temporal Transformations," in Proceedings of International Specialists Seminar on Component Performance and System Applications of Surface Acoustic Wave Devices (IEE, London, 1973), pp. 181-190.
4. D. E. Acker, SMPTE J. 83, 502 (1974).
5. F. G. Marshall, C. O. Newton, and E. G. S. Paige, IEEE Trans. Microwave Theory Tech. MTT-21, 216 (1973).
6. E. J. Staples, "U.H.F. Surface Acoustic Wave Resonators," in Proc. 28th Annual Symposium on Frequency Control, U.S. Army Electronics Command, Fort Monmouth, N.J., 1974, pp. 280-285.
7. G. Craven and D. M. Lush, Electron. Lett. 10, 218 (1974).
8. M. Redwood, R. B. Topolevsky, R. F. Mitchell, and J. S. Palfreemen, Electron. Lett. 11, 253 (1975).
9. R. C. M. Li, J. A. Alusow, and R. C. Williamson, "Surface-Wave Resonators Using Grooved Reflectors," in Proc. 29th Annual Symposium on Frequency Control, U.S. Army Electronics Command, Fort Monmouth, N.J., 1975, pp. 167-176, DDC AD-A017356/7.
10. J. Bording and K. A. Ingebrigtsen, Electron. Lett. 9, 63 (1973).
11. R. C. M. Li, R. C. Williamson, J. A. Alusow, and D. C. Flanders, "On the Performance and Limitations of the Surface-Wave Resonator Using Grooved Reflectors," in 1974 Ultrasonics Symposium Proceedings (IEEE, New York, 1974), pp. 257-262, DDC AD-A011321/7.

UNCLASSIFIED

SECURITY CLASSIFICATION OF THIS PAGE (When Data Entered)

19 REPORT DOCUMENTATION PAGE		READ INSTRUCTIONS BEFORE COMPLETING FORM	
1. REPORT NUMBER ESD-TR-76-113	2. GOVT ACCESSION NO.	3. RECIPIENT'S CATALOG NUMBER	
4. TITLE (and Subtitle) Solid State Research.	5. TYPE OF REPORT & PERIOD COVERED Quarterly Technical Summary 1 February - 30 April 1976. <i>rept.</i>		
7. AUTHOR(s) Alan L. McWhorter	6. PERFORMING ORG. REPORT NUMBER 1975:4		
9. PERFORMING ORGANIZATION NAME AND ADDRESS Lincoln Laboratory, M.I.T. P.O. Box 73 Lexington, MA 02173	8. CONTRACT OR GRANT NUMBER(s) F19628-76-C-0002		
11. CONTROLLING OFFICE NAME AND ADDRESS Air Force Systems Command, USAF Andrews AFB Washington, DC 20331	10. PROGRAM ELEMENT, PROJECT, TASK AREA & WORK UNIT NUMBERS Project No. 649L		
14. MONITORING AGENCY NAME & ADDRESS (if different from Controlling Office) Electronic Systems Division Hanscom AFB Bedford, MA 01731	12. REPORT DATE 15 May 1976		
	13. NUMBER OF PAGES 76		
	15. SECURITY CLASS. (of this report) Unclassified		
	15a. DECLASSIFICATION DOWNGRADING SCHEDULE		
16. DISTRIBUTION STATEMENT (of this Report) Approved for public release; distribution unlimited. <i>14 TN-1975-4</i> <i>16 AF-649L</i>			
17. DISTRIBUTION STATEMENT (of the abstract entered in Block 20, if different from Report)			
18. SUPPLEMENTARY NOTES None			
19. KEY WORDS (Continue on reverse side if necessary and identify by block number) solid state devices surface-wave technology imaging arrays quantum electronics photodiode devices infrared imaging materials research lasers surface-wave transducers microelectronics laser spectroscopy			
20. ABSTRACT (Continue on reverse side if necessary and identify by block number) This report covers in detail the solid state research work of the Solid State Division at Lincoln Laboratory for the period 1 February through 30 April 1976. The topics covered are Solid State Device Research, Quantum Electronics, Materials Research, Microelectronics, and Surface-Wave Technology. Funding is primarily provided by the Air Force, with additional support provided by the Army (BMDATC), ARPA (MSO, IPTO), NSF, and ERDA.			

DD FORM 1473 EDITION OF 1 NOV 65 IS OBSOLETE
1 JAN 73

* U.S. GOVERNMENT PRINTING OFFICE: 1976 600-223/(42) 63

UNCLASSIFIED

SECURITY CLASSIFICATION OF THIS PAGE (When Data Entered)

207650

yB

